Check for updates

ADVANCED HEALTHCARE MATERIALS
www.advhealthmat.de

A Multifunctional Nanostructured Hydrogel as a Platform for Deciphering Niche Interactions of Hematopoietic Stem and Progenitor Cells

*Anita Ludwig-Husemann, Peter Schertl, Ananya Shrivastava, Udo Geckle, Johanna Hafner, Frank Schaarschmidt, Norbert Willenbacher, Uwe Freudenberg, Carsten Werner, and Cornelia Lee-Thedieck**

For over half a century, hematopoietic stem cells (HSCs) have been used for transplantation therapy to treat severe hematologic diseases. Successful outcomes depend on collecting sufficient donor HSCs as well as ensuring efficient engraftment. These processes are influenced by dynamic interactions of HSCs with the bone marrow niche, which can be revealed by artificial niche models. Here, a multifunctional nanostructured hydrogel is presented as a 2D platform to investigate how the interdependencies of cytokine binding and nanopatterned adhesive ligands influence the behavior of human hematopoietic stem and progenitor cells (HSPCs). The results indicate that the degree of HSPC polarization and motility, observed when cultured on gels presenting the chemokine SDF-1α and a nanoscale-defined density of a cellular (IDSP) or extracellular matrix (LDV) $\alpha_4\beta_1$ integrin binding motif, are differently influenced on hydrogels functionalized with the different ligand types. Further, SDF-1α promotes cell polarization but not motility. Strikingly, the degree of differentiation correlates negatively with the nanoparticle spacing, which determines ligand density, but only for the cellular-derived IDSP motif. This mechanism potentially offers a means of predictably regulating early HSC fate decisions. Consequently, the innovative multifunctional hydrogel holds promise for deciphering dynamic HSPC-niche interactions and refining transplantation therapy protocols.

1. Introduction

Stem cell niches are highly specialized microenvironments that regulate stem cell behavior via biophysical and biochemical signals.[1,2] The term "niche" was coined by Schofield for the hematopoietic system in 1978.[3] Hematopoietic stem cells (HSCs) give rise to all blood cell types via differentiation. Their self-renewal is crucial to maintain the HSC pool over the entire lifetime. Both processes are tightly regulated by the microenvironment of HSCs in the bone marrow via soluble factors, cell–cell and cell–matrix interactions.[1,4,5] Adhesion molecules present on niche cells and in the extracellular matrix (ECM) retain HSCs in their niche. Integrins are a main receptor family for HSC-niche interactions. They are heterodimers of one α and one β chain. Among them, $\alpha_4\beta_1$ integrin is one of the best studied and seems to be necessary for HSC retention in the bone marrow.[6]

A. Ludwig-Husemann, P. Schertl, A. Shrivastava, F. Schaarschmidt, C. Lee-Thedieck
Institute of Cell Biology and Biophysics
Leibniz University Hannover
Herrenhäuser Str. 2, 30419 Hannover, Germany
E-mail: lee-thedieck@cell.uni-hannover.de

The ORCID identification number(s) for the author(s) of this article can be found under https://doi.org/10.1002/adhm.202304157

© 2024 The Author(s). Advanced Healthcare Materials published by Wiley-VCH GmbH. This is an open access article under the terms of the Creative Commons Attribution License, which permits use, distribution and reproduction in any medium, provided the original work is properly cited.

DOI: 10.1002/adhm.202304157

A. Ludwig-Husemann
Institute of Functional Interfaces
Karlsruhe Institute of Technology (KIT)
Hermann-von-Helmholtz-Platz 1, 76344 Eggenstein-Leopoldshafen, Germany

U. Geckle
Institute for Applied Materials – Energy Storage Systems
Karlsruhe Institute of Technology (KIT)
Hermann-von-Helmholtz-Platz 1, 76344 Eggenstein-Leopoldshafen, Germany

J. Hafner, N. Willenbacher
Institute for Mechanical Process Engineering and Mechanics
Applied Mechanics Group
Karlsruhe Institute of Technology (KIT)
Gotthard-Franz-Str. 3, 76131 Karlsruhe, Germany

U. Freudenberg, C. Werner
Leibniz Institute of Polymer Research Dresden e.V
Max Bergmann Center of Biomaterials
Hohe Str. 6, 01069 Dresden, Germany

Primary biological ligands of integrin $\alpha_4\beta_1$ are the ECM molecule fibronectin and the cellular ligand vascular cell adhesion molecule-1 (VCAM-1).[7,8] Fibronectin is a ubiquitous ECM molecule found throughout the bone marrow. In the niche, it is produced by a variety of cells including endothelial cells, stromal cells, and osteoblasts.[4,9] Fibronectin promotes HSC adhesion, migration, homing, proliferation and differentiation.[9,10] HSCs express a variety of fibronectin receptors,[9] beside $\alpha_4\beta_1$,[8,11] integrin $\alpha_5\beta_1$,[12] $\alpha_4\beta_7$,[13] $\alpha_9\beta_1$,[14] and $\alpha_V\beta_3$.[15] While the classical fibronectin receptors $\alpha_5\beta_1$ and $\alpha_V\beta_3$ bind mainly to the RGD binding motif of fibronectin,[16] $\alpha_4\beta_1$ has several binding sites in different segments of fibronectin. Among them LDV in the connecting segment 1 is the most prominent motif, which is bound with high affinity by α_4 integrins.[17]

VCAM-1 is presented by endothelial and stromal cells as well as osteoblasts in the HSC niche.[18a,b,19] The cell–cell interaction of HSCs via integrin $\alpha_4\beta_1$ to VCAM-1 expressing cells in the niche was described to enable progenitor function maintenance as well as homing and retention of HSCs in bone marrow.[20–22] Like fibronectin, VCAM-1 contains several integrin-specific binding motifs. The minimal sequence IDSP of VCAM-1 is a sequence homologue to LDV in fibronectin[23] and mediates a dynamic intercellular adhesion.[24]

Among the soluble factors, cytokines produced by cells in the niches contribute to control HSC functions including maintenance and differentiation. The chemokine stromal derived factor-1 (SDF-1) or CXCL-12, which is recognized by the receptor CXCR4, takes a central role in niche function by promoting not only HSC quiescence but also HSC migration and homing to the bone marrow niche.[25a–h,26–28]

In the niche, SDF-1 is mainly produced by perivascular cells, but also by endothelial cells or stromal cells, although to a lesser extent.[28,29] Upon secretion, SDF-1 can be bound by the ECM in the niche, more precisely by heparan sulfates. Heparan sulfates are important glycosaminoglycans of the bone marrow ECM. Besides acting in HSC retention and homeostasis, their binding of SDF-1 yields SDF-1 gradients that stimulate directed migration and homing of hematopoietic cells to the bone marrow.[30]

HSCs are regulated not only by the biochemical constituents but also the biophysical properties of the niche. For instance, it is well known that hematopoietic stem and progenitor cells (HSPCs) are sensitive to the mechanical properties of their environment.[31] The bone marrow is a heterogeneous tissue with elastic moduli in the range of 0.25–24.7 kPa in the central marrow[32] and 2–100 kPa at the inner bone surface.[33] Stiffer regions resembling the endosteal part of bone marrow favor HSC maintenance and early progenitors, while softer substrates resembling perivascular regions promote rather proliferation and differentiation.[34,35]

Similarly, the nanostructure of the environment was shown to influence HSPC adhesion, proliferation and differentiation by using nanofibrous scaffolds[36] and substrates patterned via block copolymer micelle nanolithography (BCML) that allow precise control of the lateral spacing of ligands.[37–40]

C. Werner
Center for Regenerative Therapies Dresden
Technical University Dresden
Fetscherstr. 105, 01307 Dresden, Germany

Overall, HSC niches provide an intricate network of biochemical and biophysical signals that control HSC behavior. Thereby, the various signaling cues do not operate independently but rather in concert. This is exemplified by the crosstalk of integrin $\alpha_4\beta_1$ and CXCR4 signaling, where, SDF-1 enhances $\alpha_4\beta_1$-mediated hematopoietic cell adhesion to both fibronectin and to VCAM-1.[41–43] This synergistic crosstalk is coupled to the influence of the biophysical properties of the presented signals, i.e., the stiffness of the matrix presenting the adhesion ligands, lateral spacing of adhesive motifs or the presentation and release of chemokines from the matrix. Therefore, the goal of the present work was to develop a multifunctional platform that mimics the niche in terms of parameters known to influence HSPCs: mechanical properties, release of soluble factors, and nanostructured presentation of adhesive ligands. For this purpose, a nanopatterned, cytokine-releasing hydrogel was developed. The hydrogel matrix was based on biohybrid star-shaped poly(ethylene glycol) (sPEG)-heparin hydrogels[44] that were shown before to efficiently bind and release cytokines and to be suitable for HSPC culture.[45] The hydrogels were nanopatterned with gold nanoparticles (AuNPs) via BCML, which allows to produce AuNP arrays with quasi-hexagonal order, in which the interparticle distance on the nanometer scale can be tuned by controlling the production parameters.[46] The AuNPs at the gel surface were functionalized with the minimal integrin $\alpha_4\beta_1$ recognition motifs LDV and IDSP of fibronectin and VCAM-1, respectively. The hydrogel matrix was adjusted to mimic bone marrow stiffness and loaded with SDF-1α. This carefully characterized platform allows for the first time to investigate the crosstalk of the integrin $\alpha_4\beta_1$ and CXCR4-signaling cues in dependency of biophysical parameters on HSPC behavior in terms of cell polarization, motility, proliferation, and differentiation (Figure S1, Supporting Information).

Using these nanostructured hydrogels, we demonstrate that the two explored ligand types affect the degree of polarization and motility of HSPCs differently with IDSP exhibiting more pronounced effects than LDV. The chemokine SDF-1α provided by the gel enhanced polarization but not motility, indicating independently regulated mechanisms. Finally, we show for the first time an IDSP ligand density-dependent differentiation effect on HSPCs, highlighting the exceptional function of integrin $\alpha_4\beta_1$ acting as a receptor for both, cell–matrix and cell–cell interactions, with a finely graduated microenvironmental sensory ability. Overall, we conclude that our newly established multifunctional hydrogel is particularly suited for systematic studies of HSPC niche parameters.

2. Results

2.1. Characterization of the Hydrogel

2.1.1. Successful Nanostructuring of Hydrogels for Precise Ligand Immobilization

The biohybrid hydrogels were nanostructured by the transfer of an already self-assembled AuNP array from the solid substrate, on which it was produced, to the hydrogel. We applied block copolymer micelle nanolithography to create regular AuNP

© 2024 The Author(s). Advanced Healthcare Materials published by Wiley-VCH GmbH

21922659, 2024, 22, Downloaded from https://onlinelibrary.wiley.com/doi/10.1002/adhm.202304157 by Karlsruher Institut F., Wiley Online Library on [29/11/2024]. See the Terms and Conditions (https://onlinelibrary.wiley.com/terms-and-conditions) on Wiley Online Library for rules of use; OA articles are governed by the applicable Creative Commons License

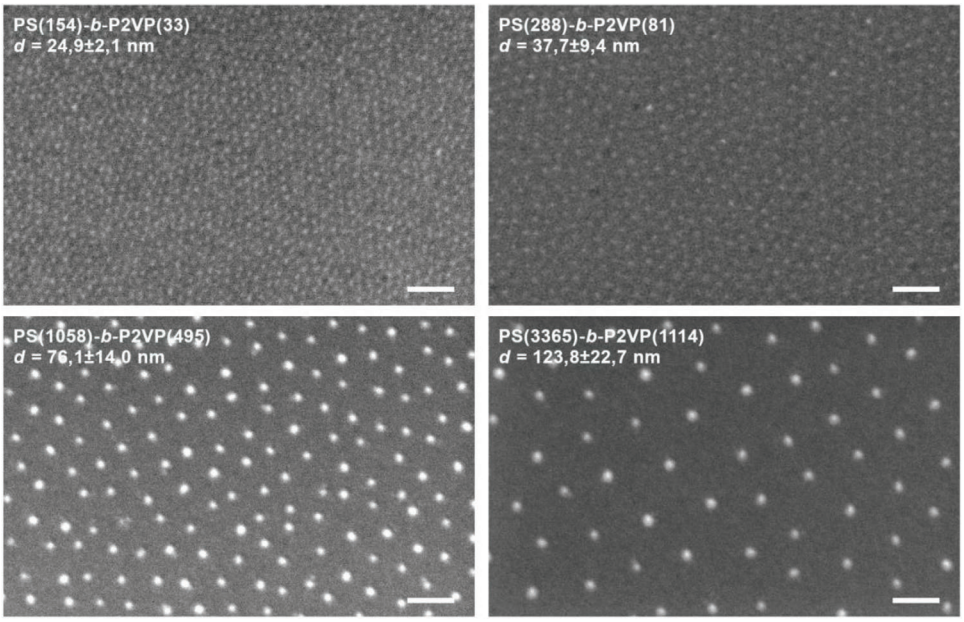

Figure 1. Representative scanning electron microscopy (SEM) images of gold nanoparticle (AuNP) arrays of defined interparticle distance (*d*) on glass. Using different diblock copolymer compositions of polystyrene (PS) and poly(2-vinylpyridine) (P2VP) in fabrication resulted in a quasi-hexagonal AuNP pattern of four non-overlapping *d*. Scale bar = 100 nm.

patterns on glass coverslips, as intermediate carriers of the nanostructure.

In order to control the lateral distribution and density of AuNPs, we utilized four different diblock copolymers (Table S1, Supporting Information), abbreviated as PS154, PS288, PS1058, and PS3365. The polymer chain length contributes significantly to an increase in the distance between the AuNPs.[47] The specific parameters for producing AuNP arrays with these four copolymers on glass substrates are listed in Table S2 in the Supporting Information.

Scanning electron microscopy (SEM) and atomic force microscopy (AFM) provided evidence that the resulting nanostructure presents a quasi-hexagonal arrangement of the AuNPs, which are of roughly uniform diameters (**Figure 1**; Figure S2, Supporting Information). The four AuNP array types on the glass substrates are characterized by significantly different mean particle distances $\langle d \rangle$, as verified by using *t*-tests. From three independent measurements as listed in **Table 1** we determined a mean $\langle d \rangle$ of 25.7 ± 1.2 nm (PS154), 37.0 ± 2.6 nm (PS288), 77.7 ± 8.4 nm (PS1058), and 124.3 ± 14.5 nm (PS3365). Those directly correspond to mean particle densities $\langle n \rangle$ ranging from ≈1755 μm^{-2} down to 75 μm^{-2} (Table 1), i.e., covering more than one order of magnitude in *n* with a maximum difference of a factor 23.5. The four mean particle distances do not overlap with respect to their scattering (Table 1), yet they are arranged adjacently in a manner that

Table 1. Particle densities of AuNP arrays on glass as characterized for three gold salt-loaded micellar solutions per polymer.

Diblock copolymer PS(*x*)-*b*-P2VP(*y*)	$d^{a)}$ [nm]	SD_d/d [%]	$\psi_6{}^{b)}$	$n^{c)}$ [μm^{-2}]
PS(154)-*b*-P2VP(33)	24.9 ± 2.1	8.4	N/A	1862.39
	26.2 ± 2.0	7.6	N/A	1682.16
	25.9 ± 2.2	8.5	N/A	1721.35
	37.7 ± 9.4	24.9	N/A	812.43
PS(288)-*b*-P2VP(81)	36.8 ± 4.5	12.2	N/A	852.66
	36.6 ± 3.4	9.3	N/A	862.00
	80.7 ± 14.6	18.1	0.55	177.31
PS(1058)-*b*-P2VP(495)	76.3 ± 14.8	19.4	0.58	198.34
	76.1 ± 14.0	18.4	0.57	199.39
	124.0 ± 28.0	22.6	0.52	75.10
PS(3365)-*b*-P2VP(1114)	125.2 ± 25.4	20.3	0.56	73.66
	123.8 ± 22.7	18.3	0.57	75.34

[a)] particle distance with standard deviation SD_d; [b)] hexagonal order; [c)] particle density.

© 2024 The Author(s). Advanced Healthcare Materials published by Wiley-VCH GmbH

21922659, 2024, 22, Downloaded from https://onlinelibrary.wiley.com/doi/10.1002/adhm.202304157 by Karlsruher Institut F., Wiley Online Library on [29/11/2024]. See the Terms and Conditions (https://onlinelibrary.wiley.com/terms-and-conditions) on Wiley Online Library for rules of use; OA articles are governed by the applicable Creative Commons License

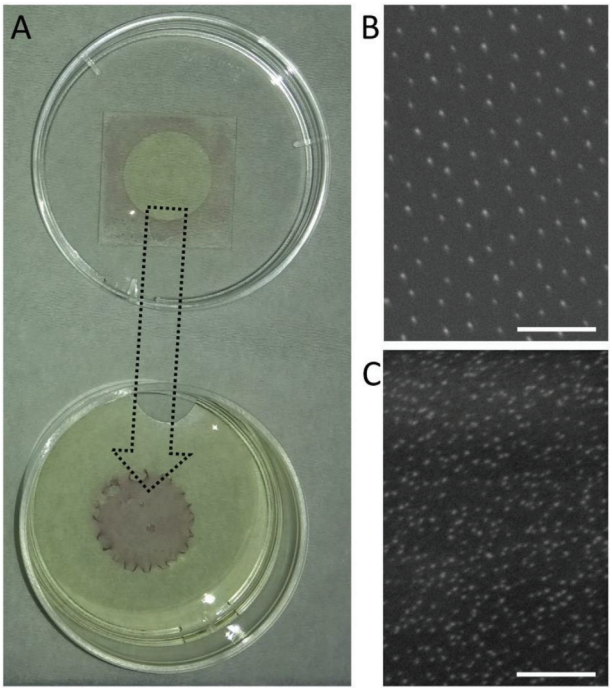

Figure 2. Transferred AuNP structure on the hydrogel surface. A) Representative photograph to qualitatively detect the hydrogel surface transferred AuNPs. Detaching (outlined arrow) the gel disc from the nanostructured coverslip transferred the AuNP array from the square carrier substrate (top) to the hydrogel surface (bottom). Immersion into an aqueous solution of Au^{3+} and $[NH_3OH]Cl$ visualized AuNPs, whose particle diameter enlarged by surface-catalyzed reduction of Au^{3+}. Particle growth leads to altered surface plasmon resonance and reflection of light – here violet. Violet colored areas indicate bound AuNPs (edge region of the coverslip and entire hydrogel surface). Coverslip size = 18 × 18 mm. B,C) Representative SEM images of an AuNP array B) on a glass substrate before transfer ($d \approx 78$ nm) and C) after transfer on the hydrogel surface. Irregular and reduced interparticle distances of the AuNPs on the gel are procedural artifacts due to massive shrinkage during dehydration and drying. Scale bar = 200 nm.

establishes a relatively continuous distance scaling from about 26–124 nm.

AuNPs on glass are bound to the hydrogel surface by thiol groups of sPEGthiol simultaneously as the gel matrix forms through the thiol-Michael addition reaction of heparin-maleimide (HM) and sPEGthiol. The AuNP array is transferred to the gel surface when detaching the swollen gels from the nanostructured glass coverslip. The electroless deposition of elemental gold on AuNPs of swollen gels visually confirms this successful transfer from the glass to the hydrogel (**Figure 2A**).

The gels used for cell experimental settings in this study have an initial solid content of ≈5% (HM+sPEGthiol relative to the prepolymer solution). In order to rule out any significant impact of the volumetric swelling of the gels on the AuNP distances on the gel surface, we determined a conservative limit on the radial size increase of gels with slightly lower solid content of 3.8%. The lower number of matrix crosslinking points at lower solid content implies a greater volumetric swelling compared to 5% solid content. For the 3.8% gels, volume swelling of the initial formed hydrogel network increased the radius by $\Delta L_{radial} \leq 6.0\%$

Table 2. Mechanical properties of the hydrogels.

	Initial solid content[a] [%]			
	3.8		5.0	
	pristine	sterilized	pristine	sterilized
ξ [nm]	13.1 ± 0.4	12.7 ± 2.9	9.3 ± 1.7	8.4 ± 1.2
G_0 [kPa]	1.9 ± 0.2	2.1 ± 1.0	5.3 ± 2.5	7.3 ± 0.3
E [kPa][b]	N/A	N/A	25.5 ± 2.6	23.6 ± 1.6

[a] HM+sPEGthiol; [b] determined in uniaxial compression of swollen gels.

and is less than the relative error of d (SD_d/d), which is lowest for the smallest distance ($d \approx 26$ nm, $SD_d/d \geq 7.6\%$, Table 1). Hence, we confirmed that volumetric gel swelling has a negligible impact on the AuNP distribution on the hydrogel surface for the used solid contents. Thus, the determined particle density of the arrays on glass coverslips approximates that on the hydrogel surface.

SEM imaging (Figure 2B,C) was applied to prove the regular pattern of AuNPs on the hydrogel surface. Due to the high-water content and accordingly massive shrinkage of the gels upon drying that is required for SEM analysis, only hydrogels decorated with an AuNP array of larger particle distances, such as those of ≈78 or ≈124 nm, could be visualized. Figure 2C clearly shows that the nanostructure is present in a uniform manner on the dry gel surface.

Additionally, time-of-flight secondary ion mass spectrometry (ToF-SIMS) analysis of dried gels with the smallest AuNP distances ($d \approx 26$ nm) could also confirm bound gold on the gel surface (Figure S3, Supporting Information). Thus, the attachment of the AuNP pattern to the gel surface generates homogeneously distributed anchor points for targeted biofunctionalization, in this study integrin $\alpha_4\beta_1$ peptide ligands. Most likely more than one peptide molecule (≈1.3 kDa) is bound by a single AuNP (diameter < 15 nm[48,49]). Due to the similar diameter of an AuNP and an integrin molecule (8–12 nm[50]), one integrin receptor binds theoretically to one peptide functionalized AuNP. Hence, the variation in AuNP density simultaneously reflects a variation in the density of potentially activated receptors in the cell membrane, and therefore allows us to study HSPC integrin $\alpha_4\beta_1$ receptor density effects.

2.1.2. Gel Elasticity Mimics the In Vivo Bone Marrow Niche

The influence of the initial solid content and the theoretically expected number of cross-links determine the mechanical characteristics summarized in **Table 2**. A higher initial solid content of 5.0% creates a higher number of covalent cross-links, and therefore a denser network with smaller mesh size (ξ = 9.3 ± 1.7 nm) and higher bulk elastic plateau shear modulus G_0 (5.3 ± 2.5 kPa) compared to a lower initial solid content of 3.8% (ξ = 13.1 ± 0.4 nm, G_0 = 1.9 ± 0.2 kPa). Because sterility is crucial for subsequent cell culture studies, the gels were sterilized in 80% v/v ethanol (EtOH). This sterilization process includes matrix shrinking and swelling, but had a negligible impact on the investigated mechanical properties, though sterilized gels revealed a slightly higher G_0 than the corresponding pristine gels (Table 2).

© 2024 The Author(s). Advanced Healthcare Materials published by Wiley-VCH GmbH

21922659, 2024, 22, Downloaded from https://onlinelibrary.wiley.com/doi/10.1002/adhm.202304157 by Karlsruher Institut F., Wiley Online Library on [29/11/2024]. See the Terms and Conditions (https://onlinelibrary.wiley.com/terms-and-conditions) on Wiley Online Library for rules of use; OA articles are governed by the applicable Creative Commons License

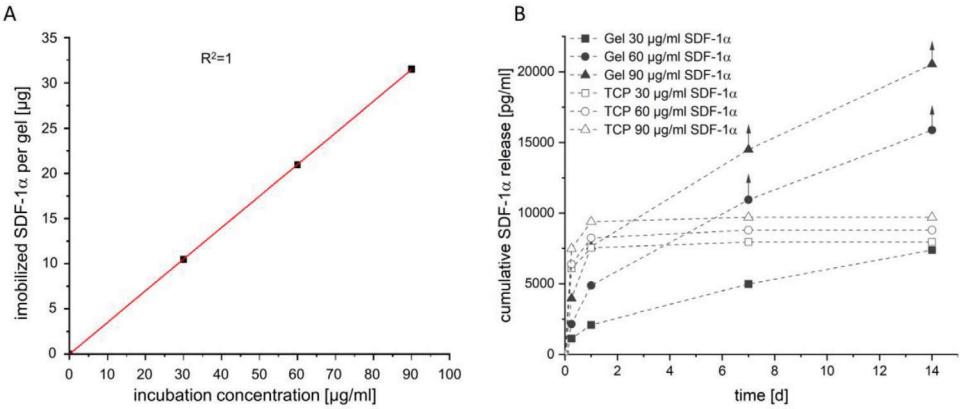

Figure 3. Immobilization and release of SDF-1α by hydrogels. A) Amount of SDF-1α immobilized per gel at different incubation concentrations (30, 60, or 90 µg mL^{-1} SDF-1α in PBS), linear regression, $R^2 = 1$. B) Cumulative release of SDF-1α in cell culture medium from loaded hydrogels over the course of 14 d at different time points. Gels and, for comparison, 1% w/v BSA-coated TCP were incubated for 22 h with 30, 60, or 90 µg mL^{-1} SDF-1α in PBS. The amount of SDF-1α in the medium supernatant after 6 h, 24 h, 7 d, and 14 d was quantified by ELISA. At measuring time points medium was completely exchanged. Arrows indicate possible higher concentrations due to reaching the upper detection limit of the ELISA. All data are presented as mean of two technical replicates.

In oscillatory shear, storage moduli dominate over loss moduli in the frequency range from 0.2 to 30 rad s^{-1} (Figure S4, Supporting Information), considered as typical elastic gel behavior. As we used the more rigid gels for cell culture studies, their bulk as well as local viscoelastic properties were examined. Uniaxial compression tests of the swollen bulk gel revealed a Young's modulus E of 25.5 ± 2.6 kPa (pristine) and 23.6 ± 1.6 kPa (sterilized), respectively.

This bulk elasticity value can be found in vivo in the region between bone marrow (0.1 kPa) and inner bone surfaces (2–100 kPa[33]) and is close to the value of in vitro secreted osteoid matrix of cultured human osteoblasts ($E \sim 27 \pm 10$ kPa[51]). Thus, the elastic Young's modulus of the hydrogel corresponds to the physiological elastic modulus of bone marrow in the osteoblast-rich endosteal zone.

For HSPCs and their cell scale of a few microns, local matrix elasticity is assumed to be the more relevant parameter for cell matrix interaction at the surface than the bulk elasticity. Microrheological examination of pristine non-swollen gels determined a local elastic plateau modulus of $G_{0,\mathrm{MPT}} = 9.0 \pm 3.6$ Pa, which is 600 times smaller than the macrorheologically determined plateau shear modulus G_0 of 5.3 ± 2.5 kPa (Table 2).

Multiple particle tracking (MPT) measurements furthermore visualized homogeneously distributed tracer particles of both fractions all over the field of view (Figure S5, Supporting Information). Tracers can freely spread in both liquids prior to crosslinking and are not limited to their initial phase (HM or sPEGthiol), indicating the formation of a homogeneous elastic network without macropores despite rapid gelation and manual mixing during production. The mean square displacement (MSD) of all tracer particles is constant over time, clearly showing that all tracers are embedded in an elastic environment. The local elastic modulus being almost three orders of magnitude smaller than the bulk elastic modulus, however, indicates that on a microscopic level densely crosslinked regions exist which are not accessible for the tracer particles.[52]

2.1.3. Matrix Loading with SDF-1α for Sustained Cytokine Delivery

The multifunctional gel system contains heparin as the natural matrix component. Heparin is structurally related to heparan sulfate. Heparin carries multiple negative charges due to sulfated groups, which electrostatically interact with clusters of positively charged amino acid residues of SDF-1α.[53] In this way, SDF-1α can be immobilized to the gel and released into the culture medium over time and at the same time, it is presented on the hydrogel surface. According to network mesh size of 8.4 ± 1.2 nm, (see Table 2) the small protein SDF-1α (about 8 kDa and 5 nm in diameter[54]) is expected to be able to penetrate the hydrogel network. We assume a homogenous distribution of SDF-1α within the hydrogel like previously shown by Prokoph et al. (2012).[67] The ability of the hydrogel matrix to bind and release SDF-1α was detected after several time intervals, by detecting concentrations of released SDF-1α in the supernatants of the hydrogels by ELISA. Gels were loaded with SDF-1α by applying different incubation concentrations (30, 60, or 90 µg mL^{-1}). Within the tested concentration range, the amount of immobilized SDF-1α follows a perfect linear correlation and therefore did not reach the saturation of binding (**Figure 3A**). The release profile monitored over the course of two weeks was driven by the concentration gradient between matrix-bound SDF-1α and the initially SDF-1α-free supernatant (exchanged cell culture medium). Figure 3B illustrates that the higher the incubation concentration – corresponding to more immobilized SDF-1α in the gel, the higher the amount of SDF-1α released per time. In contrast to the release of SDF-1α adsorbed on BSA-coated TCP that reaches a desorption plateau after 24 h, SDF-1α is continuously released from the gel into the overlaying medium over the monitored time frame. Due to the high SDF-1α binding capacity of the hydrogel, more than 99.96% SDF-1α still remains in the gel after two weeks regardless of the initially applied concentration (Figure S6, Supporting Information). This sustained release of SDF-1α from the hydrogel reservoir into the supernatant over an extended period (of at least two

© 2024 The Author(s). Advanced Healthcare Materials published by Wiley-VCH GmbH

21922659, 2024, 22, Downloaded from https://onlinelibrary.wiley.com/doi/10.1002/adhm.202304157 by Karlsruher Institut F., Wiley Online Library on [29/11/2024]. See the Terms and Conditions (https://onlinelibrary.wiley.com/terms-and-conditions) on Wiley Online Library for rules of use; OA articles are governed by the applicable Creative Commons License

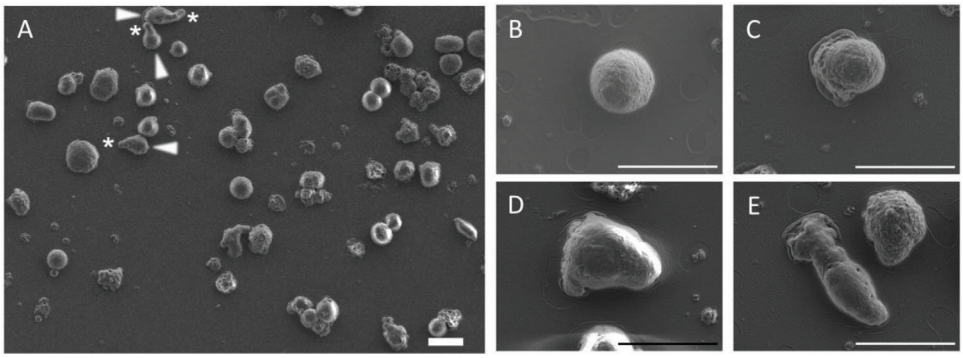

Figure 4. Variety of HSPC morphologies on nanostructured biohybrid hydrogels. Cells were cultured for 8 d on a nanostructured ($d \approx 26$ nm) and LDV peptide functionalized gel and prepared for shown SEM. A) Overview indicating the typical morphology of polarized cells with front pole (arrowhead) and uropod (star). B–E) Morphological stages between spherical and polarized. B) A completely spherical cell, C) a partially spherical cell with membrane protrusions approximating the gel surface, D) a compactly polarized cell, E) an elongated polarized cell next to a partially polarized cell. Scale bar = 10 µm.

weeks) enables permanent SDF-1α availability for HSPCs without impact of depletion or the need for regular supplementation.

2.1.4. Cell Viability on the Hydrogels

Cytocompatibility of the hydrogel was demonstrated by three complementary viability assays using the human hematopoietic model cell line KG-1a, which has a similar cell surface receptor repertoire as human HSPCs.[55] Cells were cultured for 24 h and analyzed for cell viability and functionality. In all three assays, the hydrogels proved to be at least as cytocompatible as standard culture surfaces such as TCP or glass (Figure S7A–C, Supporting Information).

2.2. Hematopoietic Stem and Progenitor Cell Behavior on Nanopatterned Biohybrid Hydrogels

2.2.1. The Dependency of HSPC Polarization and Motility on $\alpha_4\beta_1$ Integrin Ligand Type

Human HSPCs cultured on the nanopatterned hydrogels adopt different morphological phenotypes that were indicative for the direct interaction with the surface. **Figure 4** shows a SEM analysis of cell morphologies of HSPC and their progeny after 8 d of culture on a nanostructured LDV peptide functionalized hydrogel. Cells of different shapes can be seen, which can be primarily classified as spherical or polarized (elongated along the plane culture surface). Among them are cells in a polarized morphology that is typical for migrating HSPCs (Figure 4A): The front pole of the cells' long-axis is characterized by flat membrane protrusions approaching the gel surface, the lamellipodia. This is followed by the raised cell mass center and a foot-shaped tapering membrane outgrowth, the uropod, forming the rear pole. As polarization of HSPCs is a dynamic process originating from and terminated by the spherical cell shape [representative video included in the Supporting Information], observed cells were of different morphological stages. Accordingly, HSPC culture showed in parallel cell morphologies which are completely spherical (Figure 4B), spherical with some planar membrane protrusions at the substrate-facing side (Figure 4C), compactly polarized (Figure 4D), and elongated polarized (Figure 4E). All polarized morphologies increase their contact area with the underlying gel surface. It can therefore be assumed that any cell flattening up to polarization is accompanied by increased surface interaction, which potentially also has an adhesive character.

Cell polarization meaning a directional movement with the front pole ahead is a prerequisite for migration.[56] In order to describe the dynamics of cell surface interaction in terms of cell motility and whether chemokine SDF-1α stimulation facilitates motility, HSPC migratory behavior on hydrogels 48 h post seeding was recorded using time-lapse video [representative video included in the Supporting Information] and cellular tracking.

In a first step, we quantified the number of polarized cells present on the respective surface in the given time frame of 20 min. The percentage of polarized cells was below 50% on most surfaces. A tendential increase in polarized HSPCs on the control surface TCP (30,5 ± 4.7%) was detected by addition of SDF-1α at a final concentration of 90 ng mL^{-1} (34.9 ± 4.8%; **Figure 5A**). Similarly, SDF-1α had a positive effect on the polarization of the HSPC populations observed on the IDSP peptide functionalized gels (40.1 ± 5.6% vs 45.6 ± 5.2%; Figure 5B). On the LDV peptide functionalized gels, the percentage of polarized cells was slightly increased (40.4 ± 6.2% vs 43.0 ± 3.9%) when gels were loaded with SDF-1α, although not statistically different. The type of peptide used for functionalization (IDSP vs LDV) had no significant influence on the percentage of polarized cells (Figure 5B).

While the enhancing effect of SDF-1α on polarization tended to be observed for hydrogels without nanoarrays (unstructured hydrogels "non" in Figure 5C,D), the peptide ligand density based on the 4 different nanostructure types on the hydrogel surface did not numerically affect the polarization of the respective HSPC culture (Figure 5C,D). Consequently, the availability of SDF-1α already promotes the number of polarized HSPCs after 48 h culture, while the tested integrin $\alpha_4\beta_1$ peptide ligand densities are not a driver for governing polarization.

For cell motility analysis, only polarized cells which moved on the surface for the entire time period were examined. The migratory behavior of the HSPCs is described by a background flux corrected velocity vector, termed as the mean corrected velocity. To prove whether the HSPCs were migratory responsive for SDF-1α, HSPCs on TCP were stimulated with 90 ng mL^{-1}

© 2024 The Author(s). Advanced Healthcare Materials published by Wiley-VCH GmbH

21922659, 2024, 22, Downloaded from https://onlinelibrary.wiley.com/doi/10.1002/adhm.202304157 by Karlsruher Institut F., Wiley Online Library on [29/11/2024]. See the Terms and Conditions (https://onlinelibrary.wiley.com/terms-and-conditions) on Wiley Online Library for rules of use; OA articles are governed by the applicable Creative Commons License

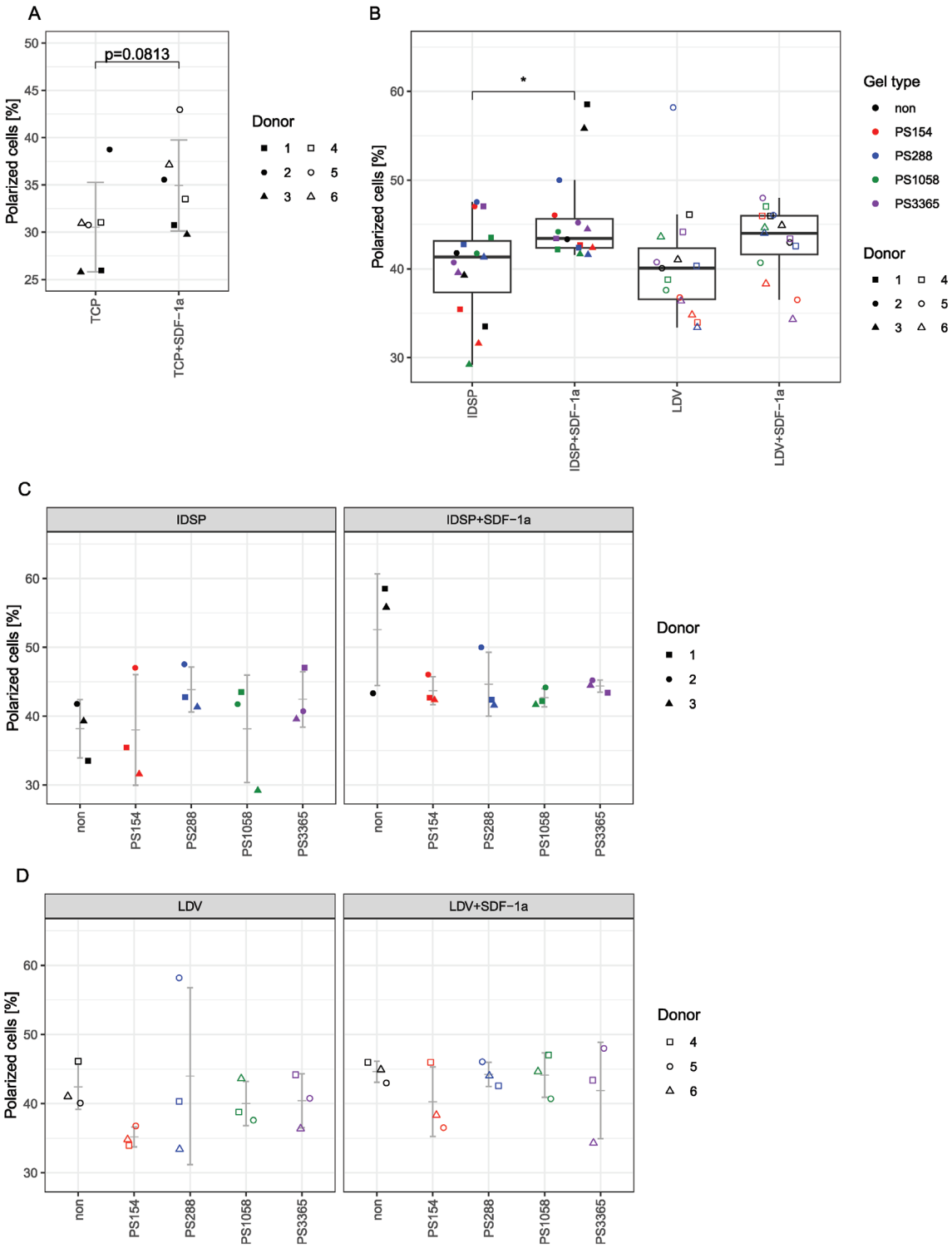

Figure 5. Proportion of polarized HSPCs influenced by SDF-1α after 48 h on different surfaces. A) Effect of SDF-1α supplementation (90 ng mL^{-1}) on the proportion of polarized HSPCs on TCP. Indicated is the mean ± SD from 6 independent experiments, same symbols indicate same experiments with cells from same donors. B) Proportion of polarized HSPCs on functionalized hydrogels. Functionalization with IDSP or LDV peptide with (+SDF-1α) and without SDF-1α loading of the gels. Boxplots summarize the data from all hydrogels displayed in (C) and (D) that were incubated with the respective peptides from 3 independent experiments of each peptide functionalization. C,D) Proportion of polarized HSPCs on different functionalized nanostructured and nonstructured hydrogels. Hydrogels with AuNP arrays (PS*) and nonstructured (non) hydrogels without AuNP array, all treated with C) IDSP or D) LDV peptides with (+SDF-1α) and without SDF-1α load. Plots indicate mean ± SD from 3 independent experiments. B–D) Same symbols indicate experiments performed with cells from same donors, colors indicate the different gel types. Statistical significance was determined via post hoc tests based on linear mixed effect models. An asterisk * indicates $p < 0{,}05$. For $0.05 < p < 0.1$ the value of p is indicated as number.

© 2024 The Author(s). Advanced Healthcare Materials published by Wiley-VCH GmbH

21922659, 2024, 22, Downloaded from https://onlinelibrary.wiley.com/doi/10.1002/adhm.202304157 by Karlsruher Institut F., Wiley Online Library on [29/11/2024]. See the Terms and Conditions (https://onlinelibrary.wiley.com/terms-and-conditions) on Wiley Online Library for rules of use; OA articles are governed by the applicable Creative Commons License

SDF-1α that reduced significantly the mean corrected velocity (0.10 ± 0.01 µm s^{-1} for TCP, 0.08 ± 0.01 µm s^{-1} for TCP+SDF-1α, **Figure 6A**).

Grouping the gels according to their peptide ligand functionalization, those without SDF-1α loading showed a tendency towards higher mean corrected velocity of cells on IDSP peptide functionalized gels (0.08 ± 0.01 µm s^{-1}) than on LDV peptide functionalized gels (0.07 ± 0.01 µm s^{-1}, Figure 6B). This difference in velocity between both integrin $\alpha_4\beta_1$ ligand types was not observed, when gels were loaded with SDF-1α. While a difference of 0.01 µm s^{-1} appears small, it corresponds to 0.6 µm min^{-1}, which means that the difference sums up to roughly one HSPC diameter within 10–15 min. Thus, within this timeframe the faster cell would have migrated one cell length further. Contrary to HSPCs on TCP, released SDF-1α from the loaded gels did not reduce the mean corrected velocity, which was similar to the group of same peptide functionalization without SDF-1α load (Figure 6B).

Most of the different nanostructures of the gel surface and the concomitant different peptide ligand densities had no direct effect on the mean corrected velocity of migrating HSPCs when comparing each peptide ligand density (−/+SDF-1α) with the respective unstructured control (Figure 6C,D). Only the PS154-structured IDSP peptide gel with SDF-1α load revealed a significant increase (0.091 ± 0.008 µm s^{-1}) of the corrected migration velocity compared to the SDF-1α loaded PS288-structured gel (0.075 ± 0.004 µm s^{-1}) and the control (0.073 ± 0.008 µm s^{-1}, Figure 6C).

2.2.2. IDSP Ligand Density Affects the Degree of Differentiation

HSPC and their progeny expressed CD49d (integrin α_4) at a stable high level over the culture period of 12 d (≈99% D0, ≈100% D6, ≈98% D12) independent of the culture conditions (Figure S8, Supporting Information). Thus, the cells were potentially receptive to both integrin $\alpha_4\beta_1$ specific adhesion motifs (IDSP or LDV) at any time of the culture period. In contrast to the stable expression of the α_4 integrin subunits, the proportion of CD184$^+$ (CXCR4) cells in freshly isolated HSPCs varied widely with $71.5 \pm 21.4\%$ ($n = 6$) and decreased continuously on all culture surfaces to less than 45% after 12 d (Figure S8, Supporting Information). This suggests that the whole HSPC population is more receptive for SDF-1α stimulation at earlier time points. To enable a possible intertwining between the addressed integrin and cytokine signaling pathway in HSPCs, co-expression of both membrane receptor molecules would be required. Therefore, we determined CD34$^+$CD49d$^+$CD184$^+$ cell frequency and additionally the mean fluorescence intensity (MFI) of CD184-APC of this subpopulation via flow cytometry in order to infer the CXCR4 response by SDF-1α binding. Frequency and MFI were significantly reduced on gels with SDF-1α loading compared to gels without SDF-1α loading for the IDSP peptide series of experiments and tended to be reduced for the LDV peptide series of experiments (D6, Figure S9, Supporting Information).

The expansion of HSPCs determined as total cell number on IDSP or LDV peptide functionalized gels and their respective controls is very similar and shows a steeper slope for the first 6 d of culture (D6) than for the subsequent second period of 6 d (D12) leading to ≈1000-fold expansion in total (Figure S10, Supporting Information). This indicates that HSPC proliferation was independent from the ligand nanostructure. The extent of differentiation of cultured HSPCs was immunophenotypically characterized by flow cytometry. Thereby, CD34 protein expression alone is not an accurate measure of the stem cell potential of HSPCs because the majority of cells are not multipotent progenitors (MPP).[57] For this reason, we distinguished HSPCs and their progeny according to their phenotype in CD34$^+$CD38$^-$CD45RA$^-$ cells as a population with high stem cell potential (HSC and MPP) and CD34$^+$CD38$^+$ cells as committed progenitors (Figures S11–S13, Supporting Information). Analytically, a phenotypic differentiation level was determined as the ratio of CD34$^+$CD38$^+$ to CD34$^+$CD38$^-$CD45RA$^-$ cell frequency, termed differentiation quotient Q. This was further normalized (Q_{norm}) to the differentiation level of the population cultured on gels with highest integrin $\alpha_4\beta_1$ ligand density (PS154) to specifically test any dependency on ligand density.

The mean Q_{norm} increased from day 6 (D6, mean = 0.87) to day 12 (D12, mean = 1.34) on gels with IDSP peptide functionalization significantly (**Figure 7A**). This is because, for the IDSP cultures after 6 d, the normalization surface PS154, which has the highest IDSP ligand density and no SDF-1α loading, exhibited the highest HSPC culture differentiation. However, after 12 d of culture, this same surface showed the lowest degree of differentiation (Figure 7B). For LDV peptide functionalized gels, the normalization surface of PS154 was the culture with the second highest degree of differentiation on analysis day 6 (Figure 7C, left). Unlike the IDSP gels, the degree of differentiation of the normalization surface PS154 remained high compared to the other surface cultures after 12 d of culture (Figure 7C, right), so that on average there was no significant difference between D6 and D12 (Figure 7A). As a result, the mean Q_{norm} for the cultures after 12 d on IDSP gels was significantly different from that on LDV gels (Figure 7A).

A closer look at the degree of differentiation of the HSPC cultures after 6 d on the surfaces with IDSP peptide functionalization reveals that the lowest degree of differentiation was exhibited by the PS3365 culture. This low degree of differentiation was statistically significant with respect to the PS154 culture (Figure 7B, left). Other low degrees of differentiation were exhibited by the non+SDF-1α culture, PS1058, and TCP culture. Additional loading of SDF-1α into PS154 nanostructured gels with IDSP peptide functionalization (PS154+SDF-1α), as well as the functionalization of PS154 nanostructures with the control peptide (PS154+scr), both resulted in a similar decrease in differentiation compared to the pronounced differentiation observed on the PS154 IDSP gel (Figure 7B, left).

For the differentiation levels of the HSPC cultures after 6 d on the surfaces with LDV peptide functionalization, it was observed that the TCP and non+SDF-1α cultures showed the lowest differentiation levels (Figure 7C, left). The lowest mean differentiation on TCP was significantly decreased compared to the two highest mean differentiations on PS154 and PS154+SDF-1α. SDF-1α loading of PS154 nanostructured gels with LDV peptide functionalization (PS154+SDF-1α) caused no discernible change in the degree of differentiation in comparison to the unloaded PS154 gel. However, in comparison to the unstructured SDF-1α-loaded gel, the differentiation was significantly increased. Noticeable

© 2024 The Author(s). Advanced Healthcare Materials published by Wiley-VCH GmbH

21922659, 2024, 22, Downloaded from https://onlinelibrary.wiley.com/doi/10.1002/adhm.202304157 by Karlsruher Institut F., Wiley Online Library on [29/11/2024]. See the Terms and Conditions (https://onlinelibrary.wiley.com/terms-and-conditions) on Wiley Online Library for rules of use; OA articles are governed by the applicable Creative Commons License

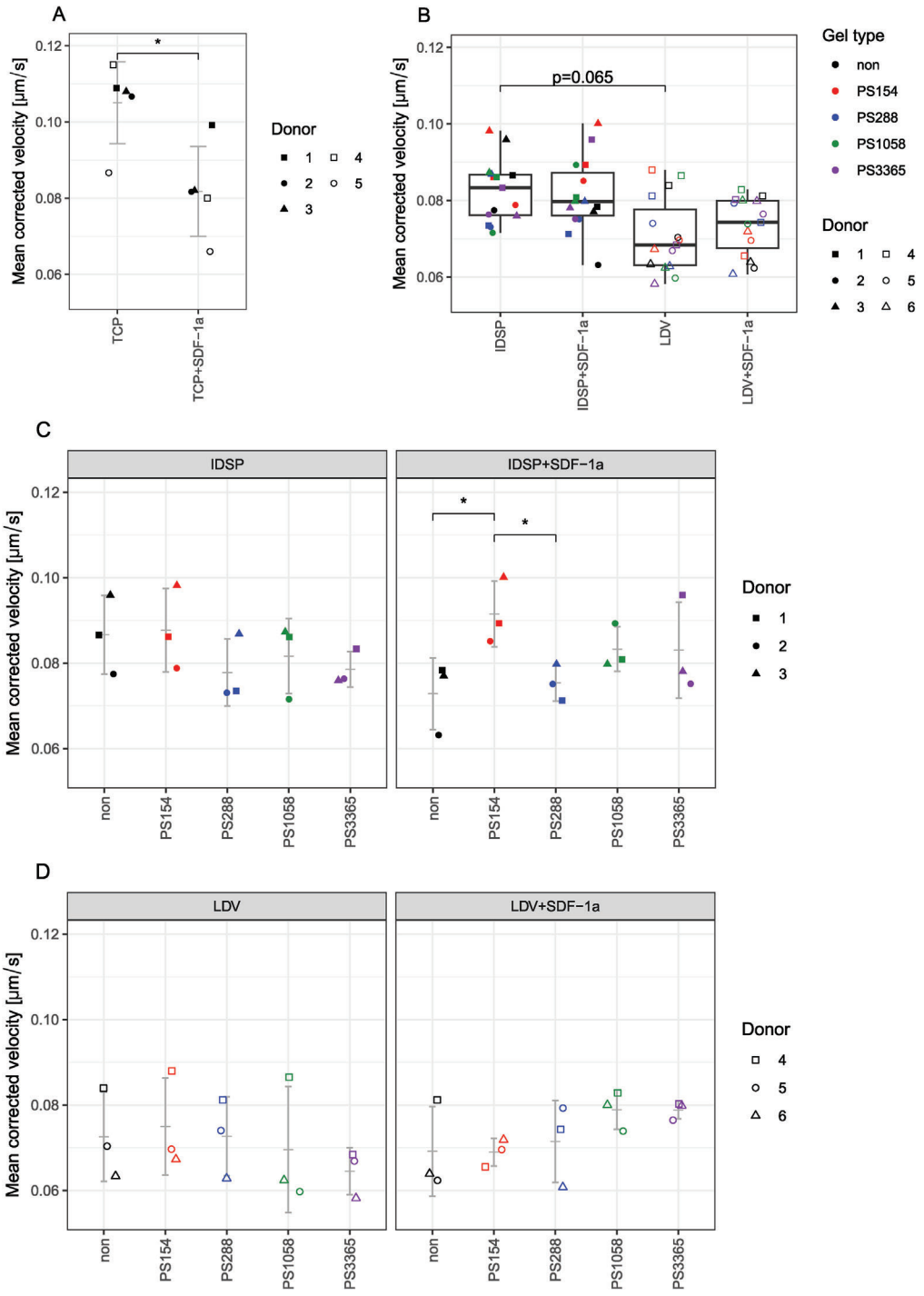

Figure 6. Influence of SDF-1α on the mean corrected velocity of migrating HSPCs on different surfaces. Time-lapse microscopy was recorded 48 h after cell seeding. Phase contrast microscopic image sequences were recorded at intervals of 30 s over a period of 20 min. For the TCP control with SDF, SDF-1α was added to the culture medium. Medium was not exchanged in the 48 h of observation. A) Effect of SDF-1α supplementation (90 ng mL^{-1}) on mean corrected velocity of migrating polarized HSPCs on TCP. Indicated is the mean $\pm$ SD from 5 independent experiments, same symbols indicate same experiments with cells from same donors. B) Mean corrected velocity of migrating polarized HSPC on functionalized hydrogels. Functionalization with IDSP or LDV peptide with (+SDF-1α) and without SDF-1α loading of the gels. Boxplots include structured hydrogels with the 4 different functionalized AuNP surfaces (PS154, PS288, PS1058, PS3365) and the nonstructured hydrogel (without nanoarray) from 3 independent experiments of each peptide functionalization. C,D) Influence of the nanostructure on the mean corrected velocity of migrating HSPC on different functionalized nanostructured and non-structured hydrogels. Hydrogels with AuNP arrays (PS*) and non-structured (non) hydrogels without AuNP array, all incubated with C) IDSP or D) LDV peptides with (+SDF-1α) and without SDF-1α load. Plots indicate mean $\pm$ SD from 3 independent experiments. B–D) Same symbols indicate experiments performed with cells from same donors, colors indicate the different gel types. For all subfigures, statistical significance was determined via post hoc tests based on linear mixed effect models.*$p < 0{,}05$, **$p < 0{,}01$, ***$p < 0005$. For $0.05 < p < 0.1$ the value of p is indicated as number.

© 2024 The Author(s). Advanced Healthcare Materials published by Wiley-VCH GmbH

21922659, 2024, 22, Downloaded from https://onlinelibrary.wiley.com/doi/10.1002/adhm.202304157 by Karlsruher Institut F., Wiley Online Library on [29/11/2024]. See the Terms and Conditions (https://onlinelibrary.wiley.com/terms-and-conditions) on Wiley Online Library for rules of use; OA articles are governed by the applicable Creative Commons License

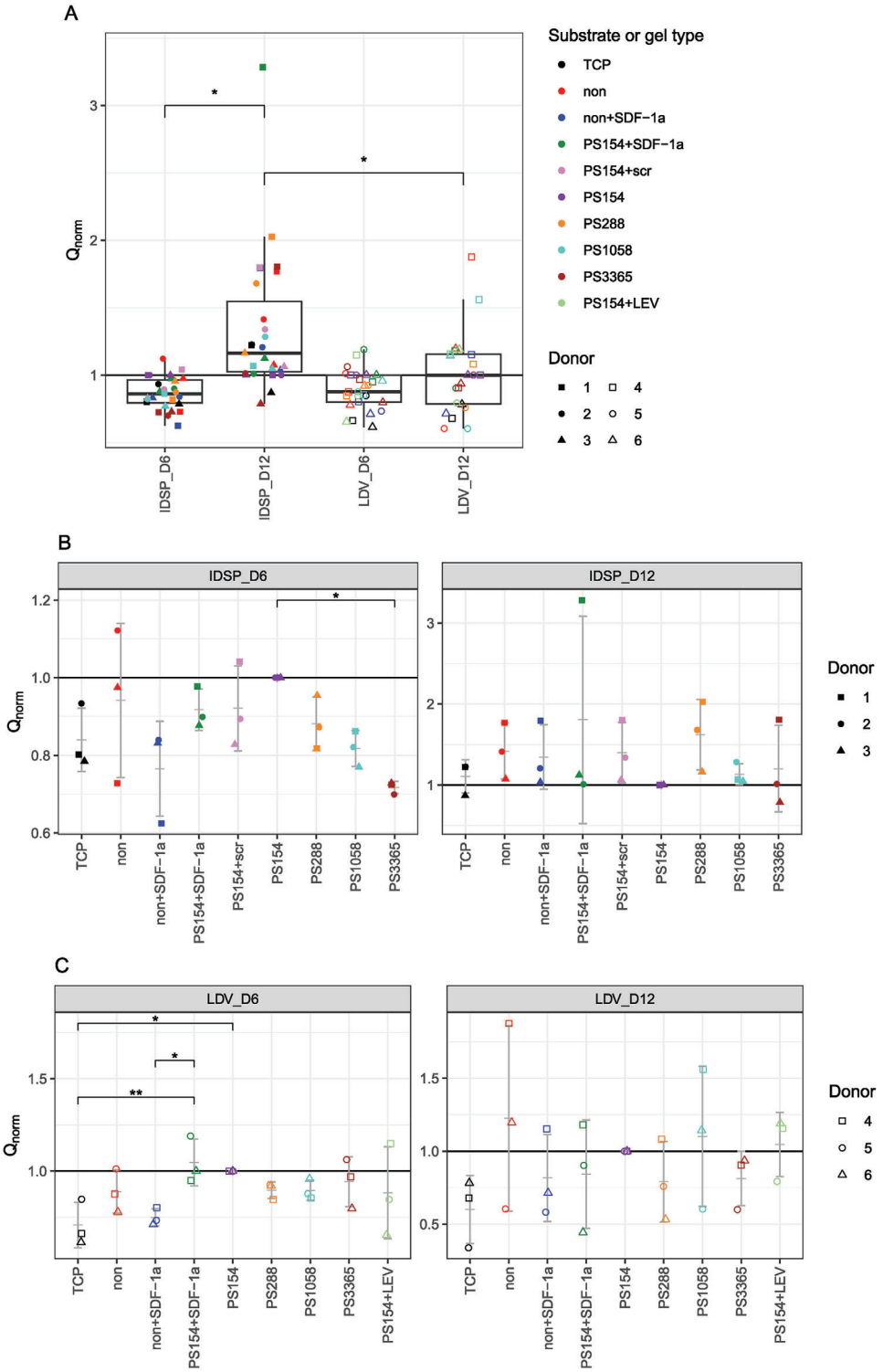

Figure 7. Degree of differentiation of HSPCs after 6 (D6) and 12 (D12) days of culture on functionalized nanostructured and unstructured hydrogels. Shown is the normalized differentiation quotient Q_{norm}, which is defined as the ratio Q of the relative frequencies of $CD34^+CD38^+$ to $CD34^+CD38^-CD45RA^-$ cells, normalized to the Q of the PS154 gel. A) Boxplots include data from 9 different surfaces (TCP, non, non+SDF-1α, PS154+SDF-1α, PS154+LEV, PS154, PS288, PS1058, and PS3365 shown in (B) and (C)) from 3 independent experiments of each peptide functionalization. B,C) Degree of differentiation of HSPCs cultured for 6 or 12 d on the different functionalized nanostructured and unstructured hydrogels. Hydrogels with AuNP arrays (PS*) and non-structured (non) hydrogels without AuNP array, all treated with IDSP or LDV peptide or the respective control peptide (scr, LEV), if necessary with SDF-1α load (+SDF-1α). Dot plots display the mean ± SD from 3 independent experiments of each peptide functionalization. A–C) Same symbols indicate experiments performed with cells from same donors, colors indicate the different substrates and gel types. Statistical significance was determined via post hoc tests based on linear mixed effect models.*p < 0,05, **p < 0,01, ***p < 0005.

© 2024 The Author(s). Advanced Healthcare Materials published by Wiley-VCH GmbH

21922659, 2024, 22, Downloaded from https://onlinelibrary.wiley.com/doi/10.1002/adhm.202304157 by Karlsruher Institut F., Wiley Online Library on [29/11/2024]. See the Terms and Conditions (https://onlinelibrary.wiley.com/terms-and-conditions) on Wiley Online Library for rules of use; OA articles are governed by the applicable Creative Commons License

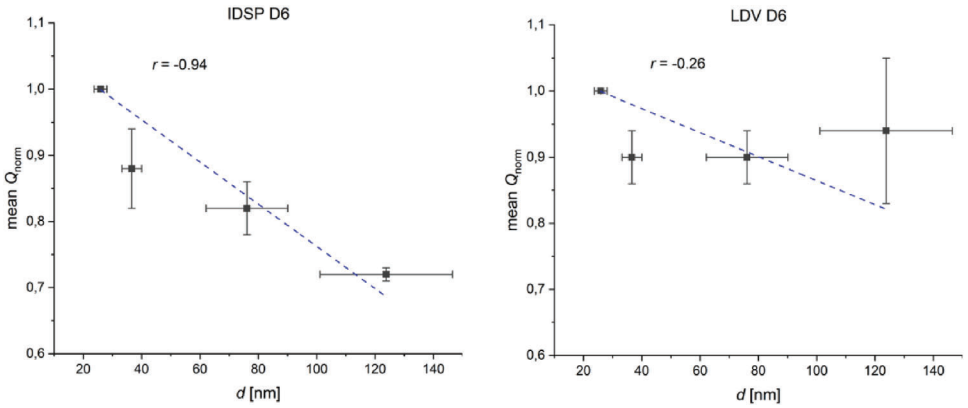

Figure 8. Correlation of the mean Q_{norm} and the mean AuNP distances (d) of nanostructured hydrogels. HSPCs were cultured for 6 d (D6) on nanostructured hydrogels with defined mean AuNP distances, nanostructure was functionalized with IDSP peptide (left) or LDV peptide (right). Shown is the mean of the normalized differentiation quotient $Q_{norm,}$ which is dependent on d and thus on the peptide ligand density. Q_{norm} is defined as the ratio Q, the relative frequencies of $CD34^+CD38^+$ to $CD34^+CD38^-CD45RA^-$ cells, normalized to the Q of the PS154 gel. Error bars represent the SD of d and Q_{norm} in x and y directions, respectively. The blue graph indicates the linear fit with x-error and shows a negative correlation for IDSP peptide functionalization (left) but not for LDV peptide functionalization (right); r = Pearson correlation coefficient.

differences with respect to the degree of differentiation after 12 d of culture were not evident for either peptide functionalization (Figure 7B right, Figure 7C right).

Furthermore, it was evaluated whether the variation of the peptide ligand density on the hydrogel surface exerts an effect on the degree of differentiation of the HSPC culture. The dependency of the normalized degree of differentiation (Q_{norm}) on the particle distance (d) of the nanostructure is graphically presented in **Figure 8**. Using a linear fit with x-error and York regression, a strong negative correlation (Pearson correlation coefficient $r = -0.94$) between Q_{norm} and d was confirmed after 6 d of culture on hydrogels with IDSP peptide functionalization. The higher the IDSP-functionalized particle distance and thus the lower the IDSP peptide density on the hydrogel, the less pronounced was the differentiation of HSPCs after 6 d of culture. Such a correlation could not be found for LDV peptide functionalization with respect to the degree of differentiation of D6 HSPC culture (Pearson correlation coefficient $r = -0.26$).

Along with the degree of differentiation showing significant differences only for D6, but no longer for D12, a similar observation was made with respect to myeloid differentiation of cultured cells (**Figure 9**). Applying the colony forming unit (CFU) assay, which allows the retrospective enumeration of early myeloid progenitors in cell populations, revealed for D6 of the LDV peptide experimental series that the total colony number of cells cultured on the SDF-1α-loaded gels (non+SDF-1α; PS154+SDF-1α) significantly increased compared to the unstructured unloaded gel (non). Beyond D6, the numbers of colonies markedly decreased until D12 irrespective of the peptide functionalization (IDSP or LDV).

3. Discussion

In the present work, we developed a multifunctional nanostructured hydrogel platform that allows to study interdependencies of adhesive ligands, cytokine binding and nanopatterning. As a proof of principle, we investigated the influence of the integrin $\alpha_4\beta_1$ and CXCR4 in dependency of nanopatterning at biomimetic stiffness on the behavior of HSPCs.

Self-renewal and differentiation of a stem cell are influenced by physical forces,[58] hence one important property of a cell culture matrix is its stiffness. The bone marrow niche stiffness, characterized by the elastic Young´s modulus E, ranges from very soft in the marrow ($E = 0.25$ kPa[32]) to very stiff at the bone inner surface ($E = 100$ kPa[33]). Therefore, we utilized a sPEG-heparin gel and varied the molar ratio to adjust the matrix elasticity.[44] We adapted the elasticity of the bulk to a constant physiological value of about 24 kPa, thus comparable to the osteoblast-rich endosteal zone of the bone marrow (≈27 ± 10 kPa[51]). This choice is based on the observation that "seeded" HSCs preferentially localize to endosteal regions as revealed by transplant studies.[59]

Interestingly, via microrheological examination the gels' local elasticity (local plateau modulus $G_{0,MPT}$) was determined 600 times smaller than the macrorheologically determined shear plateau modulus G_0. Such a discrepancy is already known for other gel systems.[60,61] One potential explanation could be that the stretched chain segments of the polymer were out of their equilibrium upon crosslinking. This localized absence of elastic restoring forces were not accessible for the tracer particles, but contributed to the macrorheologically determined elasticity. The MPT microrheological method additionally revealed a homogeneous distribution of both matrix components HM and sPEGthiol as indicated by a uniform distribution of tracer particles embedded in the gel.

Cells sense their environment at the microscale. Therefore, mechanical properties at the microscale rather than the bulk macroscale are relevant for what cells feel in contact with their matrix.[62] Given that HSPCs have a cell size of a few microns and that they adhere rather weakly to their surroundings,[63] the dimensions that they can probe lie also within the micron range. This assumption is reflected in the tight regulation of HSPCs by their microenvironment which occurs with micrometer precision.[35] Accordingly, we assume that local elasticity as measured by microrheology is more meaningful than bulk measurements for what HSPCs sense in contact to their matrix.

© 2024 The Author(s). Advanced Healthcare Materials published by Wiley-VCH GmbH

21922659, 2024, 22, Downloaded from https://onlinelibrary.wiley.com/doi/10.1002/adhm.202304157 by Karlsruher Institut F., Wiley Online Library on [29/11/2024]. See the Terms and Conditions (https://onlinelibrary.wiley.com/terms-and-conditions) on Wiley Online Library for rules of use; OA articles are governed by the applicable Creative Commons License

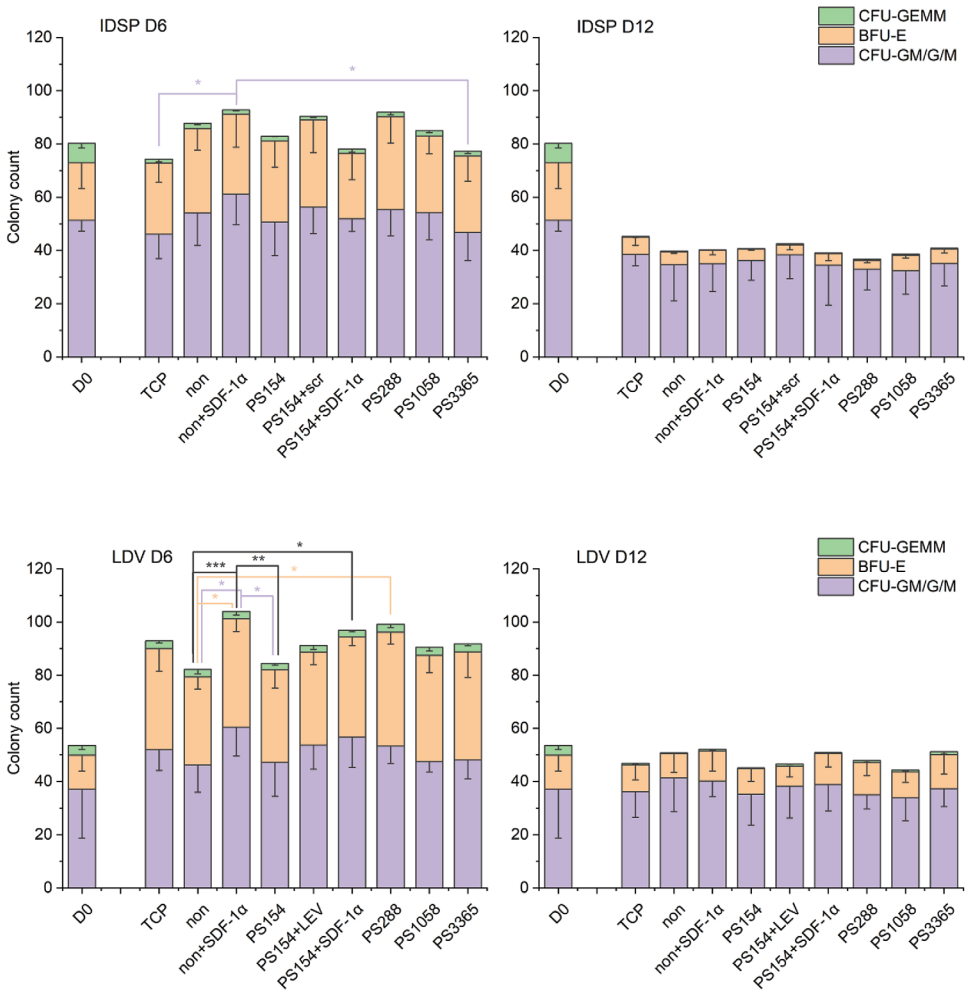

Figure 9. Myeloid colony-forming potential as determined by a colony-forming unit (CFU) assay of freshly isolated $CD34^+$ cells (D0) and the 6 d (D6) and 12 d (D12) culture on the indicated surfaces. Nonstructured (non) and nanostructured (PS*) hydrogels treated with IDSP or LDV peptide or the respective control peptide (scr, LEV), are shown. Samples loaded additionally with SDF-1α are labeled with "+SDF-1α". TCP is shown for comparison. Indicated are the absolute values of counted colony types (BFU-E; CFU-GM/G/M; CFU-GEMM) as stacked columns, which in sum indicate the total colony count, given the same seeding cell count per condition. All data are presented as mean ± SD from 3 independent experiments of each peptide functionalization. Tested for statistical significance via Tukey test of a one-way ANOVA with repeated measures within the same peptide functionalization with indicated significant differences in total colony count (black), number of CFU-GM/G/M (purple), and number of BFU-E (bright red). $*p < 0{,}05$, $**p < 0{,}01$, $***p < 0005$; colony-forming unit-granulocyte, erythrocyte, macrophage, megakaryocyte (CFU-GEMM); burst-forming unit-erythroid (BFU-E); colony-forming unit-granulocyte, macrophage (CFU-GM), -granulocyte (CFU-G), -macrophage (CFU-M).

The gels' cytokine binding function resulted from the biological compound heparin. The heparin chain is highly negatively charged and thus the molecule prominently interacts with clusters of positively charged basic amino acids on proteins.[64] In that way a variety of cytokines can be bound, which makes heparin a favored component of growth factor releasing cell culture gels with advanced medical application as cytokine releasing and/or binding grafts.[65a–g,66,67] Based on the electrostatic interactions between the polyanionic heparin and SDF-1, which has an overall positive charge of +8,[68] SDF-1α shows a high affinity for heparin ($K_d = 27.7 \times 10^{-9}$ M[53]) resulting in an enormous binding capacity of heparin (up to 6 molecules of SDF-1α bound by a single 9 kDa heparin[53]). The efficient and fast binding of SDF-1α to the sPEG-heparin biohybrid hydrogels observed in the current study reflects this high affinity of heparin to SDF-1α as shown previously for similar hydrogels.[67] The specific interaction of SDF-1α with heparin was determined to be reversible for our hydrogels, whereby the SDF-1α-loaded gels are able to provide SDF-1α permanently to cells in long-term culture (tested for a period of 2 weeks).

Beside immobilization of soluble molecules by the matrix, many heparin gels harbor covalently conjugated cell-adhesive peptides such as the RGD motif to successfully attach anchorage dependent cells.[66,67,69,70a–c] However, to gain control on the density of adhesive sequences in the developed hydrogel platform, we equipped it additionally with a nanostructure for the presentation of adhesive ligands. Here, we focused on the presentation of binding sequences that derived from VCAM-1 and fibronectin, a cellular and an extracellular ligand of integrin $\alpha_4\beta_1$, respectively. For highly motile cells such as HSPCs, the $\alpha_4\beta_1$

© 2024 The Author(s). Advanced Healthcare Materials published by Wiley-VCH GmbH

21922659, 2024, 22, Downloaded from https://onlinelibrary.wiley.com/doi/10.1002/adhm.202304157 by Karlsruher Institut F., Wiley Online Library on [29/11/2024]. See the Terms and Conditions (https://onlinelibrary.wiley.com/terms-and-conditions) on Wiley Online Library for rules of use; OA articles are governed by the applicable Creative Commons License

integrin is the essential adhesion receptor that in orchestration with the chemokine SDF-1 contributes to retention and homing to the bone marrow niche.[22,71] Although the cellular (IDSP) and the extracellular (LDV) $\alpha_4\beta_1$ integrin binding motifs are homologous sequences, we could show that these $\alpha_4\beta_1$ integrin ligand types are not equivalently influencing HSPC behavior. Accordingly, the mean velocity of polarized HSPCs revealed a tendential ligand type dependence with faster movements on gels with IDSP motif irrespective of SDF-1α availability. Integrin activation is regulated by the interaction with extracellular ligands that preferentially bind to the extended-open conformational state, termed outside-in signaling. One explanation for the observed ligand type-dependent effects can be the large difference between both ligands in their intrinsic affinity for open $\alpha_4\beta_1$. The intrinsic affinity of open $\alpha_4\beta_1$ for a fragment of human VCAM containing domain 1 and thus the motif IDSP is 14-fold higher than for the LDV motif as part of the connecting segment III of human fibronectin.[72] Further, the high-affinity, extended-open conformation of $\alpha_4\beta_1$ is indispensable for cell adhesion to VCAM as shown for leukemia cell lines.[72] Likewise, lymphoblasts withstand applied shear force better when adhered to VCAM-1 than to fibronectin,[73] though full fibronectin includes additional integrin binding motifs, such as for $\alpha_5\beta_1$, whose affinity in the open state is markedly higher compared with the open $\alpha_4\beta_1$.[72] On the developed multifunctional gels, a higher binding affinity for the IDSP motif compared to the LDV motif potentially compensates for the elastic nature of the gel matrix leading to a better "grip" to transmit HSPC cytoskeletal force and facilitate the movement on nanostructured gels.

Whereas the SDF-1α gel loading did not affect the motility of polarized HSPCs, the relative number of polarized HSPCs was clearly enhanced by SDF-1α availability on gels with IDSP motif. This finding fits previous reports showing that immobilized SDF-1α on substrates with physiological densities of VCAM-1 promotes firm integrin $\alpha_4\beta_1$-mediated HSPC adhesion and does on endothelial cells not necessarily lead to transmigration.[43,74] Another example of HSPC interactions involving the co-stimulation of $\alpha_4\beta_1$ integrin and CXCR4 is the contact with osteoblasts, SDF-1-expressing niche cells, which leads to HSPC polarization by formation of a protrusion, termed magnupodium. This is characterized by co-localization of $\alpha_4\beta_1$ and the SDF-1 receptor CXCR4 at the point of contact.[75] A physical contact with osteoblasts that involves among others the engagement of $\alpha_4\beta_1$ is found to be one crucial parameter to ensure the survival of HSPCs in vitro.[20] Moreover, polarized cell migration is proposed to be regulated by $\alpha_4\beta_1$ clustering at the cell's leading edge and the activation of a protein complex that also includes CXCR4.[76]

In addition to the outside-in model, molecular interactions with integrin cytoplasmic tails can regulate integrin activation, termed inside-out signaling, a process in which cytokine and integrin signaling converge. Several putative crosstalks between the signaling pathways mediated by $\alpha_4\beta_1$ and CXCR4 have been reported.[41,42,77a,b] A synergy of activated chemokine and integrin signaling is for example well known for T-lymphocyte adhesion. In T-lymphocytes, SDF-1 stimulation leads to a rapid and transient $\alpha_4\beta_1$ activation and further transiently potentiates restricted lateral diffusion of $\alpha_4\beta_1$ given the prerequisite of immobilized VCAM-1.[78] Interestingly, only the copresentation of SDF-1 and VCAM-1 in their immobilized form is sufficient to stimulate rapid T-lymphocyte tethering under shear flow and, moreover, only surface-bound SDF-1 triggers $\alpha_4\beta_1$ clustering.[79] In the physiological niche, the ECM serves as an immobilizer and reservoir for the soluble SDF-1. In vitro, matrix bound SDF-1 is recognized and internalized only by HSPCs interacting with the ECM, hence the adherent HSPCs.[80] The hydrogels presented here possess the inherent ability to bind specifically SDF-1α using heparin, in addition to featuring a nanostructured presentation of the VCAM-1 derived binding motif IDSP and the fibronectin-derived motif LDV. The enhanced degree of polarization of the HSPC population on SDF-1α loaded IDSP gels compared to non-loaded gels suggests the necessity of a surface-bound presentation of both ligands in a juxtaposition to trigger a synergistic cell response that is more pronounced for the IDSP motif than for the LDV sequence.

While SDF-1α showed an effect on cell polarization, its influence on cell differentiation was marginal in the presented setting. The observed trend of decreased HSPC differentiation on the nonpatterned IDSP- and SDF-1α-treated hydrogels, visible in a reduced Q_{norm} and enhanced colony formation in comparison to the gels without SDF-1α, aligns with the described function of CXCR4/SDF-1 in maintaining HSPCs in a quiescent state.[26,27] Whether the effect of SDF-1α availability was mediated by the matrix-bound or soluble form of SDF-1α or the simultaneous presence of both forms remains open. In vitro, soluble SDF-1 supplemented to the culture medium was shown to increase colony frequencies of cultivated HSPCs, whereas soluble VCAM-1 in the medium reduced colony frequencies of HSPCs after 8 d.[19] These opposing effects on the maintenance and self-renewal of HSPCs may similarly apply to the surface-bound form of the ligands, as provided by our hydrogels. Interestingly, the MFI of CD184 in $CD34^+CD49d^+CD184^+$ cells was significantly reduced on unstructured gels with SDF-1α loading compared to unstructured gels without SDF-1α loading for the IDSP peptide experiment series and tended to be reduced for the LDV peptide experiment series. As it is known that SDF-1 can trigger CXCR4 internalization after receptor activation,[81] we assume that CXCR4 is activated by SDF-1α binding on SDF-1α-loaded gels and the receptor-ligand complex is internalized. Using decellularized ECM scaffolds, Kräter et al. (2017) could show before that adherent human HSPC internalize ECM-bound SDF-1.[80]

The nanostructured IDSP and LDV gels of highest ligand density increased the degree of differentiation of HSPCs in comparison with unstructured SDF-1α loaded gels. Hence, while SDF-1α and $\alpha_4\beta_1$ integrin ligands both synergistically enhance HSPC polarization they seem to act antagonistically in terms of differentiation with SDF-1α slightly decreasing and the integrin ligands increasing the differentiation degree. Particularly concerning the cellular ligand IDSP, the regulation of ligand density could serve as a fast mechanism for adjacent niche cells to swiftly adjust $\alpha_4\beta_1$ integrin signaling in HSPCs, thereby modulating cell fate determination. For a cellular ligand, exemplary shown for the Notch ligand DLL1, ligand density rather than nanopatterning is the important feature to regulate HSPC responses.[40] In this context, we observed a strong negative correlation between the normalized degree of differentiation and particle spacing after 6 d of culture on IDSP gels. The higher the IDSP density on the hydrogel, the more pronounced was the differentiation of HSPCs. To our knowledge, this striking dependency of differentiation on

© 2024 The Author(s). Advanced Healthcare Materials published by Wiley-VCH GmbH

21922659, 2024, 22, Downloaded from https://onlinelibrary.wiley.com/doi/10.1002/adhm.202304157 by Karlsruher Institut F., Wiley Online Library on [29/11/2024]. See the Terms and Conditions (https://onlinelibrary.wiley.com/terms-and-conditions) on Wiley Online Library for rules of use; OA articles are governed by the applicable Creative Commons License

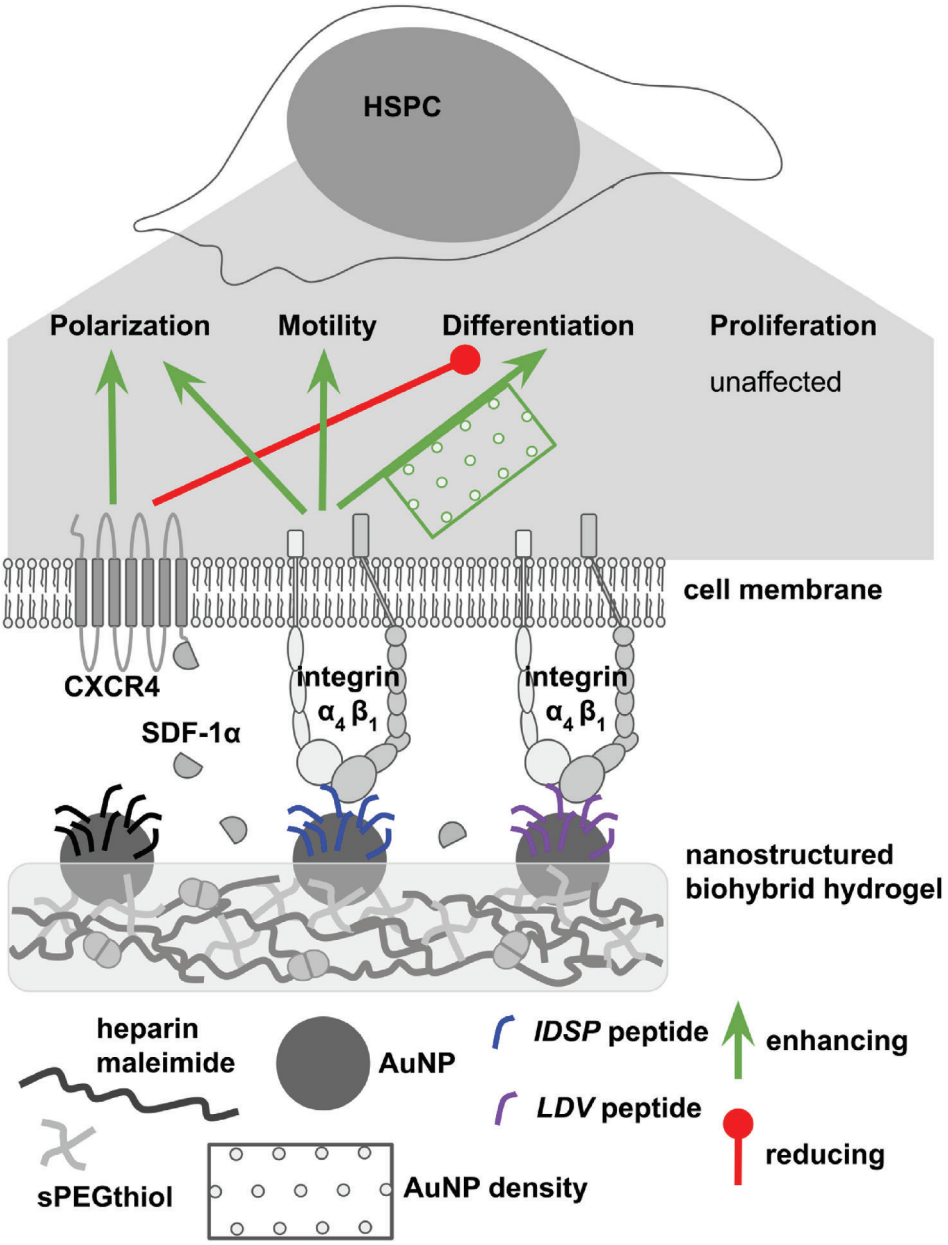

Figure 10. Schematic representation of the observed effects of the multifunctional nanostructured hydrogel on HSPCs. The gel provides essential niche-like functionalities: (I) Nanostructured presentation of the cellular IDSP or the extracellular LDV integrin $\alpha_4\beta_1$ ligand immobilized on AuNP of defined density, (II) elasticity of the hydrogel matrix transduced via AuNP-peptide-$\alpha_4\beta_1$ integrin axis, (III) Availability of SDF-1α bound and released from the matrix. These functionalities have either an increasing (green arrow) or reducing (red link) effect on the cell behavior in terms of polarization, cell motility, and degree of differentiation.

IDSP density has not been reported before. However, an integrin $\alpha_4\beta_1$ ligand density dependency is well known for differentiated cells such as lymphocytes on VCAM-1 coated surfaces, demonstrated by an increased tether frequency with increasing VCAM-1 densities above a threshold (180 sites μm^{-2})[79] and a VCAM-1 density optimum for their migration across VCAM-1 coated membranes.[73] Lymphocyte trafficking is highly regulated by adhesion and migration and can be sufficiently guided by a gradient in VCAM-1 density presented on cells. It seems conceivable that for immature cells such as HSPCs, differentiation can also be gradually regulated by a VCAM-1 density range, particularly with mean IDSP densities ranging from 75 to 1755 μm^{-2} as identified in this work on nanostructured hydrogels with a defined bulk elasticity of about 24 kPa. In this regard, it is also interesting to note that a correlation of the differentiation degree and the particle spacing, respectively ligand density, as seen for the cellular derived IDSP motif was not observed for the ECM-derived LDV motif. Several approaches with nanopatterned surfaces which were functionalized with the extracellular integrin binding motif RGD demonstrated how different ligand densities influence

© 2024 The Author(s). Advanced Healthcare Materials published by Wiley-VCH GmbH

21922659, 2024, 22, Downloaded from https://onlinelibrary.wiley.com/doi/10.1002/adhm.202304157 by Karlsruher Institut F., Wiley Online Library on [29/11/2024]. See the Terms and Conditions (https://onlinelibrary.wiley.com/terms-and-conditions) on Wiley Online Library for rules of use; OA articles are governed by the applicable Creative Commons License

HSPC adhesion, lipid raft clustering and receptor distribution in the membrane.[37,39,82] Numerous ECM proteins encompass the RGD-motif, which is recognized by eight integrin subtypes[83] among them $\alpha_5\beta_1$. During cell cycle transit of HSPCs, $\alpha_5\beta_1$ primarily mediates firm adhesion, whereas $\alpha_4\beta_1$ supports migration where both processes are inversely related to each other.[84] Apparently, the role of $\alpha_4\beta_1$ in balancing adhesion and deadhesion contributes to the complex motile behavior of HSCs in the niche that is characterized by dynamic interactions with niche factors including stromal cells.[85] Given the high abundance of stromal cells in the bone marrow,[86] HSCs are likely in a permanently alternating, transient physical contact with adjacent niche cells, mediated by ligand-receptor pairs, such as VCAM-1/$\alpha_4\beta_1$, a complex with a special kinetic binding profile.[24] The anticipated dynamic interaction of HSPCs within the niche allows multiple niche factor interactions in a short time frame. Therefore, a multifunctional culture platform providing several adjustable parameters at once is necessary to investigate their interdependencies and combined impact on the HSPCs behavior.

In conclusion, we successfully established a multifunctional nanostructured hydrogel as a platform to test HSPCs behavior in relation to the elasticity of the matrix, the binding and release of cytokines, and the nanoscale-defined density presentation of ligands. As a proof-of-principle we applied the platform to culture HSPCs on gels with a constant elasticity of about 24 kPa, while also providing the chemokine SDF-1α and presenting one of two $\alpha_4\beta_1$ integrin ligands in a nanostructured manner. As discussed and summarized in **Figure 10**, we found that these functionalities have either increasing or decreasing effects on cell functions in terms of their polarization, motility, and degree of differentiation. Notably, the cellular $\alpha_4\beta_1$ integrin motif IDSP showed more pronounced increasing effects than the extracellular motif LDV, which might be explained by the large difference in intrinsic binding affinity for the open conformation of integrin $\alpha_4\beta_1$. In addition, the SDF-1α release enhanced the relative number of polarized HSPCs, but also revealed a trend towards reduced differentiation of HSPCs. The striking correlation of the HSPC differentiation degree with the IDSP motif density may provide a mechanism to regulate early HSC fate decisions in a predictable way. We conclude that our newly established multifunctional hydrogel is particularly suited for a systematic study of single HSPC niche parameters in combination and with controlled settings.

4. Experimental Section

Block Copolymer Micelle Nanolithography: Gold nanoparticles (AuNPs) were deposited onto glass coverslips (18×18 mm, thickness 1, Carl Roth, Karlsruhe, Germany) as a temporary carrier substrate in order to achieve uniform nanostructures of the AuNPs by block copolymer micelle nanolithography (BCML),[48,87] as described previously in Kratzer, 2019.[38] Nanopatterns with an inter-particle distance of about 26, 37, 78, and 124 nm were generated by using diblock copolymers of different molecular weights (Table S1, Supporting Information) and the production parameters summarized in Table S2 in the Supporting Information. Samples from each batch of nanostructured glass coverslips were characterized by SEM with a Zeiss Merlin (Carl Zeiss SMT AG, Oberkochen, Germany) upon coating with a conductive layer of carbon of 6–10 nm thickness (Leica EM ACE600 sputter coater, Leica Microsystems GmbH, Wetzlar, Germany). The SEM images were analyzed using the ImageJ (Fiji) plug-in dot analyse2 (kindly provided by the Max- Planck-Institute for Medical Research, Department of Cellular Biophysics, Heidelberg) to precisely determine the interparticle distances and ensure the quasi-hexagonal structure. For imaging of the bound AuNP structure on the gel surface, samples of the nanostructured gels were dehydrated first in 80% v/v EtOH, then in absolute EtOH. After complete air-drying, the gels were carbon coated as described above before being subjected to SEM.

Atomic Force Measurements of AuNP Arrays on Glass Coverslips: AuNP arrays on glass coverslips were imaged with an atomic force microscope. Images were obtained in air using a TESP-V2 cantilever with Bruker JPK NanoWizard4 in Tapping Mode. The images were made at a setpoint amplitude of 4 nm, and sampling rate of 512×512 pixels with a scan rate of 1.5 Hz.

Synthesis of Heparin-Maleimide Conjugate: The synthesis protocol for the heparin-maleimide conjugate (HM) is a modified protocol based on the protocol of Tsurkan et al. 2013.[88] In brief, 1 g porcine heparin (M_W 15 000 ± 2000, Merck KGaA, Darmstadt, Germany) solution was dissolved in 3.5 mL ddH_2O. Afterwards sulfo-NHS (147 mg, 0.678 mmol, Sigma-Aldrich Chemie GmbH, Steinheim, Germany) and EDC hydrochloride (270 mg, 1.408 mmol, Sigma-Aldrich), each dissolved in ddH_2O (500 µL), were added to the heparin solution. After 20 min under constant stirring on ice, *N*-(2-aminoethyl)maleimide trifluoroacetate (115 mg, 0.452 mmol, Sigma-Aldrich), dissolved in ddH_2O (500 µL), was added. The substitution reaction on the sulfo-NHS heparin ester was carried out under constant stirring overnight at room temperature (RT). Subsequently the HM was purified by dialysis using dialysis tubes (high purity, regenerated cellulose, MWCO 8000) (Repligen Corporation, Rancho Dominguez, CA, USA). Dialysis was first performed against sodium chloride solution (1.8 L of 1 M), 3× for 1 h each. Afterwards four additional dialysis steps were performed with ddH_2O (1.8 L), with the first step overnight and all subsequent steps for 1 h. After snap-freezing the HM in liquid nitrogen, it was freeze-dried overnight and stored at −20 °C. The degree of maleimide functionalization was determined by nuclear magnetic resonance (NMR) spectroscopy using an Avance 400 MHz Spektrometer (Bruker Corporation, Billerica, MA, USA) and analyzed using MestReNova (Mestrelab Research, Santiago de Compostela, Spain).

Preparation of Nanostructured Hydrogels: For the preparation of the prepolymer solution, sPEGthiol (4arm PEG Thiol, M_W 10 000, JenKem Technology, Peking, China) as well as the HM were dissolved in phosphate buffer (0.1 M, pH 6.4). Two different concentrations of the HM (1.5 and 2 nmol μL^{-1}) were used for the prepolymer solution. Depending on the degree of functionalization of the HM – on average 5 maleimide groups per heparin molecule – the amount of sPEGthiol was calculated in such a way that maleimide and thiol groups were stoichiometrically balanced. Equal volumes of HM and sPEGthiol were used to prepare a 160 µL prepolymer solution. Immediately after mixing, the solution was pipetted in a self-made casting mould. Each component of the casting mould was made of glass and simply cohered to each other by wetting the surface with a small water droplet. The spacer consisted of two coverslips (thickness 5, 0.5–0.6 mm), one above the other. Two of these spacers were placed on a microscope slide (76×26 mm) leaving an area in between to fix a prepared nanostructured coverslip (with nanostructure pointing upward) or a blank coverslip (thickness 1, 0.13–0.16 mm) as control. The cover for the mould consisted of a long coverslip (26×40 mm, thickness 1) and a fixed round coverslip (diameter 15 mm, thickness 1) in the center. This cover was placed on top of the spacers such that the round coverslip faced to the formed gap. The prepolymer solution was pipetted in the space between the two small coverslips in the middle of the mould (≈0.8 mm thickness) until the round coverslip was fully covered. After 10 min polymerization at RT the casting mould was submerged in a petri dish filled with phosphate buffered saline (PBS). Within PBS, the casting mould could be easily disassembled. The two small coverslips on both sides of the gel remained attached to it. The gels were swollen overnight in PBS in a humidified incubator at 37 °C and 5% CO_2. After removing both coverslips from the gel disc, the diameter was adjusted by using a wad punch (diameter 15.5 mm) to fit in a 24-well cell culture plate.

The successful transfer of the AuNP arrays to the hydrogel surface was onetime verified by SEM (as described before) and ToF-SIMS and regularly

© 2024 The Author(s). Advanced Healthcare Materials published by Wiley-VCH GmbH

21922659, 2024, 22, Downloaded from https://onlinelibrary.wiley.com/doi/10.1002/adhm.202304157 by Karlsruher Institut F., Wiley Online Library on [29/11/2024]. See the Terms and Conditions (https://onlinelibrary.wiley.com/terms-and-conditions) on Wiley Online Library for rules of use; OA articles are governed by the applicable Creative Commons License

for each batch by the NH_2OH/Au^{3+} seeding.[89] In short, an aqueous solution of 0.1% w/v $HAuCl_4$ and 0.2×10^{-3} M $[NH_3OH]Cl$ was applied, in which the hydrogels were completely immersed. Successful AuNP growth was visible by a violet coloration.

For cell culture experiments the gels were sterilized with the nanostructured surface facing up in a petri dish by immersion in 80% v/v EtOH twice for 20 min each. After complete removal of the ethanol mixture, sterile PBS was slowly added to swell the gels for ≈20 min, followed by further swelling 2× for at least 20 min in PBS and transfer into a 24-well plate.

Time-of-Flight Secondary Ion Mass Spectrometry (ToF-SIMS): Hydrogels were dehydrated in a series of acetone solutions of increasing concentration (30% v/v, 50% v/v, 70% v/v, 80% v/v, 90% v/v, 100% (v/v)). To prevent swelling, PBS was used as a solvent for ≤50% v/v acetone. To prevent crystallization of the buffer salts on the surface, water was chosen as solvent for >50% v/v acetone. The dehydrated gels were subjected to critical point drying (Leica EM CPD300, with CO_2).

ToF-SIMS was performed on a TOF.SIMS5 instrument (ION-TOF GmbH, Münster, Germany) with a Bi cluster primary ion source and a reflectron type time-of-flight analyzer. UHV base pressure was $<7\times10^{-8}$ mbar. For high mass resolution the Bi source was operated in "high current bunched" mode providing short Bi^+ primary ion pulses at 25 keV energy, and a target current of 0.18 pA at 200 µs cycle time. The short pulse length of 1.1 ns allowed for high mass resolution. The primary ion beam was scanned across a 200×200 μm^2 field of view on the sample, and 128×128 data points were recorded. For charge compensation an electron flood gun providing electrons of 21 eV was applied and the secondary ion reflectron tuned accordingly. To remove top layers an in vacuo sputter cleaning was performed. Therefore, an argon cluster source was used (Ar_{1200}, 2.5 keV energy, 1 nA beam current, eroding a concentric 350×350 μm^2 field of view).

Swelling Measurements: Gels subjected to volumetric swelling degree determination were swollen for 3 d in PBS at 4 °C. The initial radius R_i directly after gel preparation (non-swollen, relaxed gel) as well as the final radius R_s after swelling were determined using photographs of the gels placed on a calibration slide with 100 µm-scale (Media Cybernetics, Inc., Rockville, MD, USA). Images were analyzed with ImageJ software (Fiji). From the radii determined, the radial swelling S_{radial} was determined and the change in length ΔL_{radial} was calculated: $S_{radial} = \frac{R_s}{R_i}$ and $\Delta L_{radial} = \frac{R_s - R_i}{R_i} \times 100$.

Macrorheology: Small amplitude oscillatory shearing measurements were performed on swollen gel discs of 1.2 mm thickness using a rotational rheometer (MCR 501, Anton Paar, Graz, Austria) with a plate-plate geometry (diameter 10 mm). Frequency sweeps were performed at 37 °C in the linear viscoelastic regime at a shear stress amplitude τ of 1 Pa, covering the frequency range of 0.1–100 rad s^{-1}. Both storage G' and loss modulus G'' were measured as a function of frequency and mean values were calculated. For each gel type, the arithmetic mean was calculated from three technical replicates. To characterize the crosslink density, the network mesh size ξ was calculated according to[69,61] using the following equation

$$\xi = \left(\frac{G_0}{k_b T}\right)^{-1/3} \quad (1)$$

where G_0 is the elastic plateau modulus, determined as the value of G' where it exhibits a constant plateau, k_B is the Boltzmann constant, and T is the temperature.

For uniaxial compression testing, gels of ≈10 mm diameter and 4 mm thickness were prepared using a cut 2 mL disposable syringe with plunger (NORM-JECT, Henke Sass Wolf GMBH, Tuttlingen, Germany). The swollen samples were tested in a tensile testing machine (Texture Analyzer TA.XTplus, Stable Micro System, Godalming, UK) by compression up to 30% strain at a compression speed of 0.5 mm s^{-1}. The strain ϵ was calculated as the ratio of the length change ΔL during compression and initial height L_0. From this, the elastic Young´s modulus E was determined as the slope of the initial linear stress-strain curve in the strain region 0–10%.

Microrheology: Mechanical and structural properties of the hydrogel matrix were analyzed by multiple particle tracking (MPT) as explained in detail in[61] and summarized here briefly. The MPT setup used is based on an inverted fluorescence widefield microscope (Axio Observer D1, Carl Zeiss) equipped with a Fluar 100× objective (numerical aperture 1.3, 100× magnification, oil immersion lens, Carl Zeiss). Green and red fluorescent non-functionalized polystyrene microspheres of 0.2 µm diameter with density 1.06 g cm^{-3} were used as tracer particles (Bangs Laboratories, USA). 2D images (field of view 127×127 µm, frame rate 50 frames s^{-1}) of the fluorescent particles were recorded using a sCMOS camera Zyla X (Andor Technology). Movies of the fluctuating microspheres were analyzed using a custom MPT routine incorporated into the software Image Processing System (Visiometrics iPS)[90] which locates the center of mass $[x(t), y(t)]$ of each particle in every picture and allows the construction of particle trajectories. From these trajectories, individual time-averaged mean square displacements (MSD) were calculated using a self-written Matlab program based on the widely used Crocker and Grier tracking algorithm[91] with $\langle \Delta r^2(\tau) \rangle = \langle [x(t+\tau) - x(t)]^2 \rangle + \langle [y(t+\tau) - y(t)]^2 \rangle$ where τ is the time lag and t the elapsed time. Tracer particles trapped in an elastic network exhibit a time-independent MSD directly related to the local elastic plateau modulus $G_{0,MPT}$ of the matrix via the relationship[92]

$$G_{0,MPT} = \frac{2k_B T}{3\pi a \left\langle \Delta r^2(\tau) \right\rangle} \quad (2)$$

with a being the tracer particle radius, k_B the Boltzmann constant, T the temperature and $\langle \Delta r^2(\tau) \rangle$ the constant MSD value.

Peptide Functionalization of the Nanostructure: Surface bound AuNPs were functionalized with integrin $\alpha_4\beta_1$ peptide ligands, which were constructs containing the adhesive LDV (C-PEG_6-EILDVPST) or IDSP (C-PEG_6-TQIDSPLN) motif. The respective control sequences were LEV (C-PEG_6-EILEVPST) and a scrambled peptide (scr, C-PEG_6-QNLSPITD; all purchased from EMC Microcollections GmbH, Tübingen, Germany). AuNP-structured and nonstructured gels were incubated with 10×10^{-6} M peptide solution in PBS (400 µL per well) for 3 h at RT. Unbound peptides were removed by washing with PBS three times for 20 min each.

Immobilization and Release of Soluble SDF-1α: SDF-1α loading of the gels was carried out after gelation. For release experiments, non-fixed hydrogel discs in 24-well culture plates previously passivated with 1% w/v BSA (Sigma-Aldrich) in PBS were incubated with 30, 60, or 90 µg mL^{-1} recombinant human SDF-1α (BioLegend Inc., San Diego, CA, USA) in PBS for 22 h in the cell incubator (37 °C, 5% CO_2, up to 95% relative humidity (RH)). The gels and control wells (BSA-coated TCP) were washed twice with PBS to remove unbound SDF-1α and RPMI 1640 medium (400 µL, Sigma Aldrich) were added. After 6 h, 24 h, 7 d and 14 d under cell culture conditions (37 °C, 5% CO_2, 95% RH), the supernatant was collected and exchanged with fresh medium. All samples were stored at −80 °C until analysis using Human SDF-1α enzyme-linked immunosorbent assay (ELISA) Kit (Thermo Fisher Scientific Inc., Waltham, MA, USA) according to the manufacturer's instructions.

It is observed that the gels did not reach saturation of loading and the release profiles were similar in the incubation concentration range of 30–90 µg mL^{-1}. Therefore, for cell culture experiments, gels were loaded with 30 µg mL^{-1} SDF-1α in PBS overnight (37 °C, 5% CO_2, 95% RH), washed once with PBS for 20 min and equilibrated for 1 h in cell-specific medium under standard cell culture conditions directly before cell seeding. For TCP motility experiments we used culture media supplemented with 90 ng mL^{-1} SDF-1α as this is the concentration measured in bone marrow aspirates of healthy subjects.[93]

Isolation of HSPCs from Human Umbilical Cord Blood: Human umbilical cord blood samples for research were obtained from DKMS Stem Cell Bank gGmbH (Dresden, Germany) after written informed consent of the mothers in accordance with the approval by the local ethics committee (Ethik-Kommission bei der Landesärztekammer Baden-Württemberg, B-F-2013-111). Mononuclear cells were isolated in less than 48 h after

© 2024 The Author(s). Advanced Healthcare Materials published by Wiley-VCH GmbH

21922659, 2024, 22, Downloaded from https://onlinelibrary.wiley.com/doi/10.1002/adhm.202304157 by Karlsruher Institut F., Wiley Online Library on [29/11/2024]. See the Terms and Conditions (https://onlinelibrary.wiley.com/terms-and-conditions) on Wiley Online Library for rules of use; OA articles are governed by the applicable Creative Commons License

21922659, 2024, 22, Downloaded from https://onlinelibrary.wiley.com/doi/10.1002/adhm.202304157 by Karlsruher Institut F., Wiley Online Library on [29/11/2024]. See the Terms and Conditions (https://onlinelibrary.wiley.com/terms-and-conditions) on Wiley Online Library for rules of use; OA articles are governed by the applicable Creative Commons License

blood collection by density gradient centrifugation with lymphocyte separation medium (PromoCell GmbH, Heidelberg, Germany). HSPCs were obtained by positive selection of $CD34^+$ cells via magnetic activated cell sorting (MACS, Miltenyi Biotec B.V. & Co. KG, Bergisch Gladbach, Germany) according to the manufacturer's instructions. The purity was assessed by flow cytometry using CD34-VioBright 515 REAfinity antibody (Miltenyi Biotec) and met ≥95% $CD34^+$ cells when used for cell experiments. $CD34^+$ cells were not pooled and originated from one cord blood sample (donor) per experiments. The donors for the IDSP and LDV experiments are different due to the limited number of cells isolated from one donor.

Cell Culture: HSPCs were maintained in Hematopoietic Progenitor Cell Expansion Medium DXF with 1% v/v Cytokine Mix E (both PromoCell GmbH, Heidelberg, Germany), referred as expansion medium. HSPCs were subjected to experimental settings immediately after isolation and cultured on the surface of the polymerized and functionalized hydrogels. For seeding the cells on top of the gels, gels were equilibrated for 1 h (37 °C, 5% CO_2, 95% RH) in expansion medium. Medium was removed and cells were seeded with a density of 2×10^4 cells in a total volume of 1 mL fresh expansion medium. On day 3 and 9 of culture, expansion medium (500 µL per well) was added. On day 6, all cells were collected for analysis and reseeded with a density of 2×10^4 cells mL^{-1} fresh expansion medium. The number of living cells were counted with a Neubauer chamber (VWR International, Radnor, USA) after staining with 0.4% v/v trypan blue (Sigma Aldrich). The human leukemia cell line KG-1a was used as a model cell line for HSPCs and utilized to establish protocols and to measure cell viability on the gels. They were purchased from the Leibniz Institute DSMZ (German Collection of Microorganisms and Cell Cultures, Braunschweig, Germany) and cultured in RPMI 1640 medium (Sigma Aldrich) with heat-treated fetal bovine serum (FBS; 20% v/v; Sigma Aldrich). All cells were cultured under standard cell culture conditions (37 °C, 5% CO_2, 95% RH).

Metabolic Activity Measurement of KG-1a by WST-1 Assay: Triplicates of unstructured hydrogels were prepared (see "Synthesis of heparin-maleimide conjugate"). The gels were placed in a 24-well plate prepared with 1 mL culture medium (RPMI 1640 + 20% heat inactivated FBS) and equilibrated for 30 min in an incubator (37 °C, 5% CO_2, up to 95% RH). After replacing the medium and incubating for additional 30 min, 700 µL of medium was added per well. As control, TCP or wells with sterile coverslips were used. After overnight incubation in the incubator, supernatants were removed and used as culture medium for 2×10^4 KG-1a cells in 100 µL in a 96-well plate. The cells were incubated for 24 h in the incubator. After addition of water soluble tetrazolium-1 (WST-1, 10 µL per well), the cells were incubated for 3 h in the incubator before measured in a plate reader (Perkin Elmer Instruments Inc., Waltham, MA, USA) at 440 nm specific wavelength and 670 nm reference wavelength. The triplicate values were averaged. From the averaged specific absorbance value of each condition the respective blank value was subtracted and reported relative to the TCP condition.

FITC-Annexin V / SYTOX AADvanced Staining of KG-1a Cells Analyzed by Flow Cytometry: Gels were prepared identically as described for the WST-1 assay. After equilibration of the gels, 1.2×10^5 KG-1a cells in culture medium (600 µL per well) were seeded and incubated overnight (37 °C, 5% CO_2, 95% RH). Subsequently the cells were transferred to reaction tubes and washed with annexin buffer (10×10^{-3} M HEPES, 140×10^{-3} M NaCl, 2.5×10^{-3} M $CaCl_2$, pH = 7.4). After centrifugation, the cells were resuspended in annexin buffer (100 µL) with SYTOX AADvanced (1×10^{-6} M, Invitrogen, Life Technologies Corporation, Eugene, OR, USA), added by 10 µL FITC-Annexin V (100 µg mL^{-1}, BioLegend Inc., San Diego, CA, USA) and stained for 15 min at RT in the dark. The samples were diluted by adding annexin buffer (200 µL) and subjected to flow cytometry analysis (BD FACSVerse, Becton Dickinson Inc., East Rutherford, NJ, USA). Single stain controls, containing heat-treated and untreated KG-1a cells, were used for compensation.

Live-Dead Staining of KG-1a for Fluorescence Microscopy: Gels were prepared identically as described for the WST-1 assay. After equilibration of the gels, 2.5×10^4 KG-1a cells were seeded per well and incubated for 24 h in medium (750 µL RPMI 1640 + 20% heat inactivated FBS). Cells were stained with the cell viability imaging kit (Roche Diagnostics GmbH, Penzberg, Germany) according to the manufacturer's instructions. In brief, staining solution was added (250 µL per well) and incubated for 30 min in the incubator. Then the samples were imaged using an Axio Observer.Z1 microscope (Carl Zeiss AG, Oberkochen, Germany) and analyzed by using ImageJ (reduction of the inhomogeneous background via "Auto Local Threshold"; "Watershed"; "Analyze Particles" with 20 pixels size minimum and 0.1–1.0 circularity).

Preparation of HSPCs on Hydrogels for SEM Imaging: $CD34^+$ cells were cultured for 8 d on hydrogels with the highest LDV peptide density (PS154). For imaging HSPCs adherent on gels the cells were fixed with 0.625% v/v glutaraldehyde in PBS for 40 min. Subsequently the gel was incubated with 50% v/v EtOH in PBS for 10 min and afterwards with 80% v/v EtOH in H_2O. The final dehydration was carried out in absolute EtOH. The air-dried gel was coated with a carbon layer of about 7 nm thickness (Leica EM ACE600 sputter coater) and subjected to SEM (Zeiss Merlin).

Analysis of Cell Polarization and Motility on Hydrogels: After 48 h of seeding $CD34^+$ cells on TCP, nanostructured and unstructured gels without and with SDF-1α loading, cell polarization and motility was analyzed over a period of 20 min at intervals of 30 s using an Axio Observer.Z1 (Carl Zeiss AG) with an incubator (XL-5 2000; 5% CO_2, 90% RH) and a heating insert (M24 2000; 37 °C). Before starting microscopy, inter-well regions were filled with sterile PBS to minimize the thermal gradient between the well center and edge.[94] The SDF-1α availability for cells on TCP was adjusted to a final concentration of 90 ng mL^{-1} SDF-1α by adding SDF-1α solution (1 µL of 90 µg mL^{-1}) to the medium before analysis by microscopy. Image analysis at time points 0, 10, and 20 min was performed by classifying cells as either polarized or spherical based on their aspect ratio. For this purpose, the algorithm Cellpose for cellular segmentation and the Fiji plug-in "labels to ROI"[95,96] were applied. First, phase contrast images were analyzed with Cellpose. For the segmentation, the pretrained cyto model was used with built-in model estimation of the diameter of cells for each image. For cells grown on TCP, the cyto3 model was used. Labels set by Cellpose were saved as.png files which were further analyzed using the Fiji plug-in "labels to ROI". The aspect ratios were measured by Fiji using fitted ellipses to the regions of interest (ROI) where the length of the major axis is divided through the minor axis. Cells were considered to be polarized when having an aspect ratio of 1.3 or higher.

Cell motility was followed by time-lapse movies, in which 12 polarized cells per movie were manually tracked with the ImageJ software using the plug-in *Manual Tracking*. Subsequently the text file output was imported into the *Chemotaxis and Migration Tool 1.01* (Ibidi) for further analysis and graphical display. In the motion track diagram, the cells clearly showed a preferred migratory direction that was caused by a different background flux for each surface. To make the measurements comparable, the mean corrected velocity of the cells was determined. For this, the velocity of the background flux ($\overrightarrow{v_{bf}}$) was subtracted from the measured velocity of the individual polarized cells ($\overrightarrow{v_i}$) of the motion profile at each timestamp (t) according to the following equation

$$\overrightarrow{v_{i,cor}}(t) = \overrightarrow{v_i}(t) - \overrightarrow{v_{bf}} \text{ with } \overrightarrow{v_{bf}} = \begin{pmatrix} v_{bf,x} \\ v_{bf,y} \end{pmatrix} = \frac{\sum_{i=1}^{N} \langle \overrightarrow{v_i}(t) \rangle}{N} \quad (3)$$

Flow Cytometry Analysis of HSPC Surface Marker Expression: On day 0 (D0), day 6 (D6), and day 12 (D12) of culture, HSPCs were washed and first incubated in Viobility 405/452 (Miltenyi Biotec; diluted 1:200 in PBS) for 10 min at RT in the dark. Subsequently, the cells were stained with a mixture of either anti-human CD34-VioBright 515 (dilution 1:100), anti-human CD38-APC (1:75), anti-human CD45RA-PE (1:75), or anti-human CD34-VioBright 515 (1:100), anti-human CD184-APC (1:75), anti-human CD49d-PE (1:75) (all REAfinity antibodies from Miltenyi Biotec) in staining buffer (0.5% w/v BSA and 2×10^{-3} M EDTA in PBS) for 30 min at 37 °C in the dark. In parallel, control staining comprising the respective isotype controls and unstained samples were performed as well. Afterwards, the samples were washed once with buffer and analyzed on a MACSQuant Analyzer 10 (Miltenyi Biotec). A manual compensation was run using compensation beads (anti-REA, Miltenyi Biotec) and CD34-VioBright 515 or CD45RA-PE, respectively. The acquired data were analyzed using FlowJo

 © 2024 The Author(s). Advanced Healthcare Materials published by Wiley-VCH GmbH

10.6.1 (Becton, Dickinson and Company). Thereby all intensity values that were >99% of the isotype control intensity values were defined as positive signals, so that false positive signals were limited to 1%. By defining $CD34^+CD38^-CD45RA^-$ cells as population with high stem cell potential and $CD34^+CD38^+$ cells as committed progenitors, the differentiation ratio $Q = f_{34^+38^+}/f_{34^+38^-45RA^-}$ was chosen, where f is the relative frequency of the respective population. Q is thus considered as a degree of differentiation. Additional normalization to the Q of the PS154 gel resulted in a normalized differentiation quotient Q_{norm}

$$Q_{norm,IDSP}(X) = \frac{Q(X)}{Q(PS154 + IDSP)} \text{ and } Q_{norm,LDV}(X) = \frac{Q(X)}{Q(PS154 + LDV)} \quad (4)$$

Colony Forming Unit (CFU) Assay: To measure the myeloid differentiation and proliferation ability of the hydrogel cultured HSPCs, CFU assays were performed that allow the enumeration of early myeloid progenitors in a cell population. In this assay, cells are seeded in a semisolid medium, in which early myeloid progenitors give rise to colonies produced by differentiation and proliferation from the individual input progenitor cells. The colonies can be discriminated microscopically in different colony types, which refer to different subtypes of myeloid progenitor cells.[97] For this, 1500 collected cells on culture day 0 (D0), 6 (D6), and 12 (D12) were resuspended in Iscove's modified Dulbecco's medium containing 2% FBS, then mixed with MethoCult H4434 Classic (both Stemcell Technologies) and plated as triplicates in a concentration of ≈500 cells per mL in a 35 mm cell culture dish. After 10 (D0) or 14 (D6, D12) days under standard cell culture conditions, the types of formed colonies were evaluated by light microscopy (Axio Vert.A1, Carl Zeiss AG) according to the "Atlas of human hematopoietic colonies from cord blood" (Stemcell Technologies, 2010) and enumerated manually by means of a gridded scoring dish.

Statistical Analysis: Data represent means ± standard deviation (SD) of at least three independent experiments unless stated otherwise.

Statistical analysis of the percentage of polarized cells (Figure 5) and mean corrected velocities (Figure 6) was performed by fitting linear mixed effect models, in order to account for the three-factorial layout with repeated measurements obtained from the same donors. The models contained the three factors gel type, SDF (with/without), peptide (IDSP, LDV) and their interactions as fixed effects, and contained random effects for factor donor and its interaction with factors gel type and SDF. Normalized differentiation quotients (Q_{norm}; Figure 7) were $\log_{10}$ transformed and analyzed in linear mixed effect models allowing for different variances between day 6 and day 12. The model of the joint analysis of day 6 and 12 contained the three factors gel type, peptide (IDSP, LDV) and day (D6, D12) and their interactions as fixed effects, and random effects donor, and its interaction with day. For the residuals of each model, the assumptions of normality and homogeneity of variance were checked using quantile–quantile plots amended with confidence bands for the residuals. Based on estimated means and standard errors obtained from these fitted models, pairwise mean comparisons (between levels of SDF and peptide) and Tukey test (between gel types) were performed using Kenward–Roger degrees of freedom. The analysis was performed in R 4.4.0 (R Core Team, 2024), using the add-on packages lme4, nlme, hnp, emmeans, and ggplot2.

Remaining statistical analyses were (Figures 3,8, and 9; Figures S8 and S9, Supporting Information) performed using OriginPro 2021 (OriginLab Corporation, MA, USA). Statistical significance was tested within the same peptide functionalization with Tukey tests following a one-way ANOVA with repeated measures. Significant differences were indicated in the figures with one to three asterisks as follows: *($p < 0.05$), **($p < 0.01$), ***($p < 0.005$). For $0.05 < p < 0.1$, the value of p was indicated in the figure.

Supporting Information

Supporting Information is available from the Wiley Online Library or from the author.

Acknowledgements

The authors thank Dr. Alexander Welle and the Karlsruhe Nano Micro Facility (Karlsruhe Institute of Technology, Eggenstein-Leopoldshafen) for the ToF-SIMS measurements. This work was supported by NanoMatFutur program of the German Federal Ministry of Education and Research (BMBF; FKZ 13N12968 and 13XP5076A). This project has also received funding from the European Research Council (ERC) under the European Union's Horizon 2020 research and innovation programme (grant agreement No. 757490). This work has been carried out within the framework of the SMART BIOTECS alliance between the Technische Universität Braunschweig and the Leibniz Universität Hannover. This initiative is supported by the Ministry of Science and Culture (MWK) of Lower Saxony, Germany. The AFM was funded by the Deutsche Forschungsgemeinschaft (DFG, German Research Foundation) – 420502711. The ZEISS MERLIN SEM was financially supported by the Federal Ministry of Economics and Technology on the basis of a decision by the German Bundestag within the BMBF grant no. 03ET6017.

Open access funding enabled and organized by Projekt DEAL.

Conflict of Interest

The authors declare no conflict of interest.

Data Availability Statement

The data that support the findings of this study are available from the corresponding author upon reasonable request.

Keywords

block copolymer micelle nanolithography, differentiation, hematopoietic stem cells, integrins, multifunctionality, nanostructures, two dimensional hydrogels

Received: November 24, 2023
Revised: June 10, 2024
Published online: June 25, 2024

[1] S. J. Morrison, A. C. Spradling, *Cell* **2008**, *132*, 598.
[2] D. T. Scadden, *Cell* **2014**, *157*, 41.
[3] R. Schofield, *Blood Cells* **1978**, *4*, 7.
[4] C. Lee-Thedieck, P. Schertl, G. Klein, *Adv. Drug Delivery Rev.* **2021**, *181*, 114069.
[5] A. Mendelson, P. S. Frenette, *Nat. Med.* **2014**, *20*, 833.
[6] J. M. P. Grenier, C. Testut, C. Fauriat, S. J. C. Mancini, M. Aurrand-Lions, *Front. Immunol.* **2021**, *12*, 756231.
[7] a) S. Shishido, H. Bönig, Y.-M. Kim, *Front. Oncol.* **2014**, *4*, 99; b) C. Wu, A. J. Fields, B. A. Kapteijn, J. A. McDonald, *J. Cell Sci.* **1995**, *108 (Pt 2)*, 821; c) M. J. Elices, L. Osborn, Y. Takada, C. Crouse, S. Luhowskyj, M. E. Hemler, R. R. Lobb, *Cell* **1990**, *60*, 577.
[8] D. A. Williams, M. Rios, C. Stephens, V. P. Patel, *Nature* **1991**, *352*, 438.
[9] F. Wirth, A. Lubosch, S. Hamelmann, I. A. Nakchbandi, *Cells* **2020**, *9*, 2717.
[10] a) B. M. M. Sagar, S. Rentala, P. N. V. Gopal, S. Sharma, A. Mukhopadhyay, *Biochem. Biophys. Res. Commun.* **2006**, *350*, 1000; b) J. A. Cancelas, *Methods Mol. Biol.* **2011**, *750*, 187; c) A. von Au, M. Vasel, S. Kraft, C. Sens, N. Hackl, A. Marx, P. Stroebel, J. Hennenlotter, T. Todenhöfer, A. Stenzl, S. Schott, H.-P. Sinn, A. Wetterwald, J. L. Bermejo, M. G. Cecchini, I. A. Nakchbandi, *Neoplasia* **2013**, *15*, 925.

© 2024 The Author(s). Advanced Healthcare Materials published by Wiley-VCH GmbH

21922659, 2024, 22, Downloaded from https://onlinelibrary.wiley.com/doi/10.1002/adhm.202304157 by Karlsruher Institut F., Wiley Online Library on [29/11/2024]. See the Terms and Conditions (https://onlinelibrary.wiley.com/terms-and-conditions) on Wiley Online Library for rules of use; OA articles are governed by the applicable Creative Commons License

[11] a) T. Yokota, K. Oritani, H. Mitsui, K. Aoyama, J. Ishikawa, H. Sugahara, I. Matsumura, S. Tsai, Y. Tomiyama, Y. Kanakura, Y. Matsuzawa, *Blood* **1998**, *91*, 3263; b) A. G. Arroyo, J. T. Yang, H. Rayburn, R. O. Hynes, *Immunity* **1999**, *11*, 555.
[12] P. K. Wierenga, E. Weersing, B. Dontje, G. de Haan, R. van Os, *Bone Marrow Transplant.* **2006**, *38*, 789.
[13] G. Bungartz, S. Stiller, M. Bauer, W. Müller, A. Schippers, N. Wagner, R. Fässler, C. Brakebusch, *Blood* **2006**, *108*, 1857.
[14] a) J. Grassinger, D. N. Haylock, M. J. Storan, G. O. Haines, B. Williams, G. A. Whitty, A. R. Vinson, C. L. Be, S. Li, E. S. Sørensen, P. P. L. Tam, D. T. Denhardt, D. Sheppard, P. F. Choong, S. K. Nilsson, *Blood* **2009**, *114*, 49; b) T. D. Schreiber, C. Steinl, M. Essl, H. Abele, K. Geiger, C. A. Müller, W. K. Aicher, G. Klein, *Haematologica* **2009**, *94*, 1493.
[15] T. Umemoto, M. Yamato, J. Ishihara, Y. Shiratsuchi, M. Utsumi, Y. Morita, H. Tsukui, M. Terasawa, T. Shibata, K. Nishida, Y. Kobayashi, B. G. Petrich, H. Nakauchi, K. Eto, T. Okano, *Blood* **2012**, *119*, 83.
[16] a) M. Leiss, K. Beckmann, A. Girós, M. Costell, R. Fässler, *Curr. Opin. Cell Biol.* **2008**, *20*, 502; b) M. Pfaff, K. Tangemann, B. Müller, M. Gurrath, G. Müller, H. Kessler, R. Timpl, J. Engel, *J. Biol. Chem.* **1994**, *269*, 20233.
[17] a) A. P. Mould, J. A. Askari, S. E. Craig, A. N. Garratt, J. Clements, M. J. Humphries, *J. Biol. Chem.* **1994**, *269*, 27224; b) A. Komoriya, L. J. Green, M. Mervic, S. S. Yamada, K. M. Yamada, M. J. Humphries, *J. Biol. Chem.* **1991**, *266*, 15075; c) E. A. Wayner, N. L. Kovach, *J. Cell Biol.* **1992**, *116*, 489.
[18] a) K. Jacobsen, J. Kravitz, P. W. Kincade, D. G. Osmond, *Blood* **1996**, *87*, 73; b) G. Lisignoli, S. Toneguzzi, A. Piacentini, S. Cristino, L. Cattini, F. Grassi, A. Facchini, *J. Cell. Physiol.* **2004**, *198*, 388.
[19] N. Mende, A. Jolly, G. I. Percin, M. Günther, M. Rostovskaya, S. M. Krishnan, R. A. J. Oostendorp, A. Dahl, K. Anastassiadis, T. Höfer, C. Waskow, *Blood* **2019**, *134*, 1214.
[20] Y. Jung, J. Wang, A. Havens, Y. Sun, J. Wang, T. Jin, R. S. Taichman, *Cytokine* **2005**, *32*, 155.
[21] a) J. Teixidó, M. E. Hemler, J. S. Greenberger, P. Anklesaria, *J. Clin. Invest.* **1992**, *90*, 358; b) P. J. Simmons, B. Masinovsky, B. M. Longenecker, R. Berenson, B. Torok-Storb, W. M. Gallatin, *Blood* **1992**, *80*, 388; c) T. Papayannopoulou, C. Craddock, B. Nakamoto, G. V. Priestley, N. S. Wolf, *Proc. Natl. Acad. Sci. USA* **1995**, *92*, 9647; d) T. Papayannopoulou, G. V. Priestley, B. Nakamoto, V. Zafiropoulos, L. M. Scott, *Blood* **2001**, *98*, 2403; e) M. Vermeulen, F. L. Pesteur, M.-C. Gagnerault, J.-Y. Mary, F. Sainteny, F. Lepault, *Blood* **1998**, *92*, 894.
[22] L. M. Scott, G. V. Priestley, T. Papayannopoulou, *Mol. Cell. Biol.* **2003**, *23*, 9349.
[23] a) J. M. Clements, P. Newham, M. Shepherd, R. Gilbert, T. J. Dudgeon, L. A. Needham, R. M. Edwards, L. Berry, A. Brass, M. J. Humphries, *J. Cell Sci.* **1994**, *107 (Pt 8)*, 2127; b) E. Y. Jones, K. Harlos, M. J. Bottomley, R. C. Robinson, P. C. Driscoll, R. M. Edwards, J. M. Clements, T. J. Dudgeon, D. I. Stuart, *Nature* **1995**, *373*, 539; c) J. H. Wang, R. B. Pepinsky, T. Stehle, J. H. Liu, M. Karpusas, B. Browning, L. Osborn, *Proc. Natl. Acad. Sci. USA* **1995**, *92*, 5714; d) P. Newham, S. E. Craig, G. N. Seddon, N. R. Schofield, A. Rees, R. M. Edwards, E. Y. Jones, M. J. Humphries, *J. Biol. Chem.* **1997**, *272*, 19429.
[24] X. Zhang, S. E. Craig, H. Kirby, M. J. Humphries, V. T. Moy, *Biophys. J.* **2004**, *87*, 3470.
[25] a) R. Miao, V. Y. Lim, N. Kothapalli, Y. Ma, J. Fossati, S. Zehentmeier, R. Sun, J. P. Pereira, *Front. Immunol.* **2020**, *11*, 600127; b) O. Kollet, A. Spiegel, A. Peled, I. Petit, T. Byk, R. Hershkoviz, E. Guetta, G. Barkai, A. Nagler, T. Lapidot, *Blood* **2001**, *97*, 3283; c) T. Ara, K. Tokoyoda, T. Sugiyama, T. Egawa, K. Kawabata, T. Nagasawa, *Immunity* **2003**, *19*, 257; d) T. Lapidot, A. Dar, O. Kollet, *Blood* **2005**, *106*, 1901; e) X. Shang, J. A. Cancelas, L. Li, F. Guo, W. Liu, J. F. Johnson, A. Ficker, D. Daria, H. Geiger, N. Ratner, Y. Zheng, *J. Biol. Chem.* **2011**, *286*, 24068; f) M. Sharma, F. Afrin, N. Satija, R. P. Tripathi, G. U. Gangenahalli, *Stem Cells Dev.* **2011**, *20*, 933; g) A. Greenbaum, Y.-M. S. Hsu, R. B. Day, L. G. Schuettpelz, M. J. Christopher, J. N. Borgerding, T. Nagasawa, D. C. Link, *Nature* **2013**, *495*, 227; h) C.-Y. Lai, S. Yamazaki, M. Okabe, S. Suzuki, Y. Maeyama, Y. Iimura, M. Onodera, S. Kakuta, Y. Iwakura, M. Nojima, M. Otsu, H. Nakauchi, *Stem Cells* **2014**, *32*, 1929.
[26] Y. Nie, Y.-C. Han, Y.-R. Zou, *J. Exp. Med.* **2008**, *205*, 777.
[27] Y.-S. Tzeng, H. Li, Y.-L. Kang, W.-C. Chen, W.-C. Cheng, D.-M. Lai, *Blood* **2011**, *117*, 429.
[28] T. Sugiyama, H. Kohara, M. Noda, T. Nagasawa, *Immunity* **2006**, *25*, 977.
[29] a) L. Ding, S. J. Morrison, *Nature* **2013**, *495*, 231; b) N. Asada, Y. Kunisaki, H. Pierce, Z. Wang, N. F. Fernandez, A. Birbrair, A. Ma'ayan, P. S. Frenette, *Nat. Cell Biol.* **2017**, *19*, 214; c) G. M. Crane, E. Jeffery, S. J. Morrison, *Nat. Rev. Immunol.* **2017**, *17*, 573.
[30] a) R. Roberts, J. Gallagher, E. Spooncer, T. D. Allen, F. Bloomfield, T. M. Dexter, *Nature* **1988**, *332*, 376; b) P. Gupta, J. B. McCarthy, C. M. Verfaillie, *Blood* **1996**, *87*, 3229; c) F. Di Giacomo, D. Lewandowski, E. Cabannes, V. Nancy-Portebois, M. Petitou, S. Fichelson, P.-H. Romeo, *Haematologica* **2012**, *97*, 491; d) B. Saez, F. Ferraro, R. Z. Yusuf, C. M. Cook, V. W. C. Yu, A. Pardo-Saganta, S. M. Sykes, R. Palchaudhuri, A. Schajnovitz, S. Lotinun, S. Lymperi, S. Mendez-Ferrer, R. D. Toro, R. Day, R. Vasic, S. S. Acharya, R. Baron, C. P. Lin, Y. Yamaguchi, A. J. Wagers, D. T. Scadden, *Blood* **2014**, *124*, 2937; e) D. Papy-Garcia, P. Albanese, *Glycoconjugate J.* **2017**, *34*, 377; f) T. Netelenbos, J. van den Born, F. L. Kessler, S. Zweegman, P. A. Merle, J. W. van Oostveen, J. J. Zwaginga, P. C. Huijgens, A. M. Dräger, *Leukemia* **2003**, *17*, 175; g) T. Netelenbos, J. van den Born, F. L. Kessler, S. Zweegman, P. C. Huijgens, A. M. Drager, *J. Leukocyte Biol.* **2003**, *74*, 1035; h) A. Dar, O. Kollet, T. Lapidot, *Exp. Hematol.* **2006**, *34*, 967.
[31] C. Lee-Thedieck, J. P. Spatz, *Biomater. Sci.* **2014**, *2*, 1548.
[32] L. E. Jansen, N. P. Birch, J. D. Schiffman, A. J. Crosby, S. R. Peyton, *J. Mech. Behav. Biomed. Mater.* **2015**, *50*, 299.
[33] I. L. Ivanovska, J. Swift, K. Spinler, D. Dingal, S. Cho, D. E. Discher, *Mol. Biol. Cell* **2017**, *28*, 2010.
[34] a) J. Holst, S. Watson, M. S. Lord, S. S. Eamegdool, D. V. Bax, L. B. Nivison-Smith, A. Kondyurin, L. Ma, A. F. Oberhauser, A. S. Weiss, J. E. J. Rasko, *Nat. Biotechnol.* **2010**, *28*, 1123; b) S. S. Kumar, J.-H. Hsiao, Q.-D. Ling, I. Dulinska-Molak, G. Chen, Y. Chang, Y. Chang, Y. H. Chen, D.-C. Chen, S.-T. Hsu, A. Higuchi, *Biomaterials* **2013**, *34*, 7632; c) J.-W. Shin, A. Buxboim, K. R. Spinler, J. Swift, D. A. Christian, C. A. Hunter, C. Léon, C. Gachet, P. C. D. P. Dingal, I. L. Ivanovska, F. Rehfeldt, J. A. Chasis, D. E. Discher, *Cell Stem Cell* **2014**, *14*, 81; d) B. R. Chitteti, M. A. Kacena, S. L. Voytik-Harbin, E. F. Srour, *J. Immunol. Methods* **2015**, *425*, 108; e) J. S. Choi, B. A. C. Harley, *Sci. Adv.* **2017**, *3*, e1600455.
[35] H. Li, Q. Luo, W. Shan, S. Cai, R. Tie, Y. Xu, Y. Lin, P. Qian, H. Huang, *Cell Mol. Life Sci.* **2021**, *78*, 5881.
[36] K.-N. Chua, C. Chai, P.-C. Lee, Y.-N. Tang, S. Ramakrishna, K. W. Leong, H.-Q. Mao, *Biomaterials* **2006**, *27*, 6043.
[37] E. Altrock, C. A. Muth, G. Klein, J. P. Spatz, C. Lee-Thedieck, *Biomaterials* **2012**, *33*, 3107.
[38] D. Kratzer, A. Ludwig-Husemann, K. Junges, U. Geckle, C. Lee-Thedieck, *Front. Mater.* **2019**, *5*, 81.
[39] C. A. Muth, C. Steinl, G. Klein, C. Lee-Thedieck, *PLoS One* **2013**, *8*, e54778.
[40] A.-L. Winkler, J. von Wulffen, L. Rödling, A. Raic, I. Reinartz, A. Schug, R. Gralla-Koser, U. Geckle, A. Welle, C. Lee-Thedieck, *Adv. Funct. Mater.* **2017**, *27*, 1606495.
[41] A. Hidalgo, F. Sanz-Rodriguez, J. L. Rodriguez-Fernández, B. Albella, C. Blaya, N. Wright, C. Cabañas, F. Prósper, J. C. Gutierrez-Ramos, J. Teixidó, *Exp. Hematol.* **2001**, *29*, 345.
[42] F. Sanz-Rodríguez, A. Hidalgo, J. Teixidó, *Blood* **2001**, *97*, 346.
[43] A. Peled, V. Grabovsky, L. Habler, J. Sandbank, F. Arenzana-Seisdedos, I. Petit, H. Ben-Hur, T. Lapidot, R. Alon, *J. Clin. Invest.* **1999**, *104*, 1199.

© 2024 The Author(s). Advanced Healthcare Materials published by Wiley-VCH GmbH

21922659, 2024, 22, Downloaded from https://onlinelibrary.wiley.com/doi/10.1002/adhm.202304157 by Karlsruher Institut F., Wiley Online Library on [29/11/2024]. See the Terms and Conditions (https://onlinelibrary.wiley.com/terms-and-conditions) on Wiley Online Library for rules of use; OA articles are governed by the applicable Creative Commons License

[44] U. Freudenberg, Y. Liang, K. L. Kiick, C. Werner, *Adv. Mater.* **2016**, *28*, 8861.
[45] D. Gvaramia, E. Müller, K. Müller, P. Atallah, M. Tsurkan, U. Freudenberg, M. Bornhäuser, C. Werner, *Biomaterials* **2017**, *138*, 108.
[46] a) S. V. Graeter, J. Huang, N. Perschmann, M. López-García, H. Kessler, J. Ding, J. P. Spatz, *Nano Lett.* **2007**, *7*, 1413; b) T. Lohmüller, D. Aydin, M. Schwieder, C. Morhard, I. Louban, C. Pacholski, J. P. Spatz, *Biointerphases* **2011**, *6*, MR1; c) J. Guasch, J. Diemer, H. Riahinezhad, S. Neubauer, H. Kessler, J. P. Spatz, *Chem. Mater.* **2016**, *28*, 1806.
[47] a) R. Glass, M. M. ller, J. P. Spatz, *Nanotechnology* **2003**, *14*, 1153; b) M. Arnold, E. A. Cavalcanti-Adam, R. Glass, J. Blümmel, W. Eck, M. Kantlehner, H. Kessler, J. P. Spatz, *Chemphyschem* **2004**, *5*, 383.
[48] J. P. Spatz, S. Mössmer, C. Hartmann, M. Möller, T. Herzog, M. Krieger, H.-G. Boyen, P. Ziemann, B. Kabius, *Langmuir* **2000**, *16*, 407.
[49] G. Kästle, H.-G. Boyen, F. Weigl, G. Lengl, T. Herzog, P. Ziemann, S. Riethmüller, O. Mayer, C. Hartmann, J. P. Spatz, M. Möller, M. Ozawa, F. Banhart, M. G. Garnier, P. Oelhafen, *Adv. Funct. Mater.* **2003**, *13*, 853.
[50] a) E. M. Erb, K. Tangemann, B. Bohrmann, B. Müller, J. Engel, *Biochemistry* **1997**, *36*, 7395; b) J. P. Xiong, T. Stehle, B. Diefenbach, R. Zhang, R. Dunker, D. L. Scott, A. Joachimiak, S. L. Goodman, M. A. Arnaout, *Science* **2001**, *294*, 339; c) J.-P. Xiong, T. Stehle, R. Zhang, A. Joachimiak, M. Frech, S. L. Goodman, M. A. Arnaout, *Science* **2002**, *296*, 151.
[51] A. J. Engler, S. Sen, H. L. Sweeney, D. E. Discher, *Cell* **2006**, *126*, 677.
[52] C. Oelschlaeger, J. Marten, F. Péridont, N. Willenbacher, *J. Rheol.* **2022**, *66*, 749.
[53] R. Sadir, F. Baleux, A. Grosdidier, A. Imberty, H. Lortat-Jacob, *J. Biol. Chem.* **2001**, *276*, 8288.
[54] M. P. Crump, J. H. Gong, P. Loetscher, K. Rajarathnam, A. Amara, F. Arenzana-Seisdedos, J. L. Virelizier, M. Baggiolini, B. D. Sykes, I. Clark-Lewis, *EMBO J.* **1997**, *16*, 6996.
[55] C. Lee-Thedieck, N. Rauch, R. Fiammengo, G. Klein, J. P. Spatz, *J. Cell Sci.* **2012**, *125*, 3765.
[56] F. Sánchez-Madrid, M. A. del Pozo, *EMBO J.* **1999**, *18*, 501.
[57] R. Majeti, C. Y. Park, I. L. Weissman, *Cell Stem Cell* **2007**, *1*, 635.
[58] K. H. Vining, D. J. Mooney, *Nat. Rev. Mol. Cell Biol.* **2017**, *18*, 728.
[59] a) S. K. Nilsson, H. M. Johnston, J. A. Coverdale, *Blood* **2001**, *97*, 2293; b) Y. Xie, T. Yin, W. Wiegraebe, X. C. He, D. Miller, D. Stark, K. Perko, R. Alexander, J. Schwartz, J. C. Grindley, J. Park, J. S. Haug, J. P. Wunderlich, H. Li, S. Zhang, T. Johnson, R. A. Feldman, L. Li, *Nature* **2009**, *457*, 97; c) C. Lo Celso, H. E. Fleming, J. W. Wu, C. X. Zhao, S. Miake-Lye, J. Fujisaki, D. Côté, D. W. Rowe, C. P. Lin, D. T. Scadden, *Nature* **2009**, *457*, 92; d) B. Guezguez, C. J. V. Campbell, A. L. Boyd, F. Karanu, F. L. Casado, C. Di Cresce, T. J. Collins, Z. Shapovalova, A. Xenocostas, M. Bhatia, *Cell Stem Cell* **2013**, *13*, 175.
[60] a) P. Pawelzyk, N. Mücke, H. Herrmann, N. Willenbacher, *PLoS One* **2014**, *9*, e93194; b) C. Oelschlaeger, F. Bossler, N. Willenbacher, *Biomacromolecules* **2016**, *17*, 580.
[61] J. Roether, S. Bertels, C. Oelschlaeger, M. Bastmeyer, N. Willenbacher, *PLoS One* **2018**, *13*, e0207397.
[62] L. Smith, S. Cho, D. E. Discher, *Semin. Cell Dev. Biol.* **2017**, *71*, 84.
[63] P. Zhang, C. Zhang, J. Li, J. Han, X. Liu, H. Yang, *Stem Cell Res. Ther.* **2019**, *10*, 327.
[64] I. Capila, R. J. Linhardt, *Angew. Chem., Int. Ed.* **2002**, *41*, 390.
[65] a) S. Cai, Y. Liu, X. Zheng Shu, G. D. Prestwich, *Biomaterials* **2005**, *26*, 6054; b) G. Tae, M. Scatena, P. S. Stayton, A. S. Hoffman, *J. Biomater. Polym. Ed.* **2006**, *17*, 187; c) W. I. Choi, M. Kim, G. Tae, Y. H. Kim, *Biomacromolecules* **2008**, *9*, 1698; d) U. Freudenberg, A. Zieris, K. Chwalek, M. V. Tsurkan, M. F. Maitz, P. Atallah, K. R. Levental, S. A. Eming, C. Werner, *J. Controlled Release* **2015**, *220*, 79; e) A. van Janse Rensburg, N. H. Davies, A. Oosthuysen, C. Chokoza, P. Zilla, D. Bezuidenhout, *Acta Biomater.* **2017**, *49*, 89; f) N. Lohmann, L. Schirmer, P. Atallah, E. Wandel, R. A. Ferrer, C. Werner, J. C. Simon, S. Franz, U. Freudenberg, *Sci. Transl. Med.* **2017**, *9*, 386; g) C. He, H. Ji, Y. Qian, Q. Wang, X. Liu, W. Zhao, C. Zhao, *J. Mater. Chem. B* **2019**, *7*, 1186.
[66] A. Zieris, K. Chwalek, S. Prokoph, K. R. Levental, P. B. Welzel, U. Freudenberg, C. Werner, *J. Controlled Release* **2011**, *156*, 28.
[67] S. Prokoph, E. Chavakis, K. R. Levental, A. Zieris, U. Freudenberg, S. Dimmeler, C. Werner, *Biomaterials* **2012**, *33*, 4792.
[68] A. Amara, O. Lorthioir, A. Valenzuela, A. Magerus, M. Thelen, M. Montes, J. L. Virelizier, M. Delepierre, F. Baleux, H. Lortat-Jacob, F. Arenzana-Seisdedos, *J. Biol. Chem.* **1999**, *274*, 23916.
[69] U. Freudenberg, A. Hermann, P. B. Welzel, K. Stirl, S. C. Schwarz, M. Grimmer, A. Zieris, W. Panyanuwat, S. Zschoche, D. Meinhold, A. Storch, C. Werner, *Biomaterials* **2009**, *30*, 5049.
[70] a) A. Zieris, S. Prokoph, K. R. Levental, P. B. Welzel, M. Grimmer, U. Freudenberg, C. Werner, *Biomaterials* **2010**, *31*, 7985; b) M. V. Tsurkan, K. Chwalek, M. Schoder, U. Freudenberg, C. Werner, *Bioconjugate Chem.* **2014**, *25*, 1942; c) Y. D. P. Limasale, P. Atallah, C. Werner, U. Freudenberg, R. Zimmermann, *Adv. Funct. Mater.* **2020**, *30*, 2000068.
[71] a) M. P. Rettig, G. Ansstas, J. F. DiPersio, *Leukemia* **2012**, *26*, 34; b) D. Karpova, J. K. Ritchey, M. S. Holt, G. Abou-Ezzi, D. Monlish, L. Batoon, S. Millard, G. Spohn, E. Wiercinska, E. Chendamarai, W. Yang, S. Christ, L. Gehrs, L. G. Schuettpelz, K. Dembowsky, A. R. Pettit, M. P. Rettig, H. Bonig, J. F. DiPersio, *Blood* **2017**, *129*, 2939.
[72] J. Li, T. A. Springer, *J. Cell Biol.* **2018**, *217*, 397.
[73] P. Y. Chan, A. Aruffo, *J. Biol. Chem.* **1993**, *268*, 24655.
[74] Y. Vagima, K. Lapid, O. Kollet, P. Goichberg, R. Alon, T. Lapidot, *Methods Mol. Biol.* **2011**, *750*, 277.
[75] T. Bessy, A. Candelas, B. Souquet, K. Saadallah, A. Schaeffer, B. Vianay, D. Cuvelier, S. Gobaa, C. Nakid-Cordero, J. Lion, J.-C. Bories, N. Mooney, T. Jaffredo, J. Larghero, L. Blanchoin, L. Faivre, S. Brunet, M. Théry, *J. Cell Biol.* **2021**, *220*, 11.
[76] O. Jung, D. M. Beauvais, K. M. Adams, A. C. Rapraeger, *J. Cell Sci.* **2019**, https://doi.org/10.1242/jcs.232645.
[77] a) D. A. Williams, Y. Zheng, J. A. Cancelas, *"Rho GTPases and Regulation of Hematopoietic Stem Cell Localization", in Small GTPases in Disease, Part B*, (Eds: W. E. Balch, C. J. Der, A. Hall), Elsevier, **2008**, pp. 365–393; b) J. M. Petty, C. C. Lenox, D. J. Weiss, M. E. Poynter, B. T. Suratt, *J. Immunol.* **2009**, *182*, 604.
[78] A. Sosa-Costa, S. Isern de Val, S. Sevilla-Movilla, K. J. E. Borgman, C. Manzo, J. Teixidó, M. F. Garcia-Parajo, *J. Biol. Chem.* **2016**, *291*, 21053.
[79] V. Grabovsky, S. Feigelson, C. Chen, D. A. Bleijs, A. Peled, G. Cinamon, F. Baleux, F. Arenzana-Seisdedos, T. Lapidot, Y. van Kooyk, R. R. Lobb, R. Alon, *J. Exp. Med.* **2000**, *192*, 495.
[80] M. Kräter, A. Jacobi, O. Otto, S. Tietze, K. Müller, D. M. Poitz, S. Palm, V. M. Zinna, U. Biehain, M. Wobus, T. Chavakis, C. Werner, J. Guck, M. Bornhauser, *Sci. Rep.* **2017**, *7*, 2549.
[81] a) S. Scala, *Clin. Cancer Res.* **2015**, *21*, 4278; b) F. Sadri, Z. Rezaei, M. Fereidouni, *Mol. Biol. Rep.* **2022**, *49*, 3307.
[82] C. Lee-Thedieck, J. P. Spatz, *Macromol. Rapid Commun.* **2012**, *33*, 1432.
[83] B. S. Ludwig, H. Kessler, S. Kossatz, U. Reuning, *Cancers* **2021**, *13*, 1711.
[84] A. Gothot, O. Giet, S. Huygen, Y. Beguin, *Leuk. Lymph.* **2003**, *44*, 1379.
[85] S. Upadhaya, O. Krichevsky, I. Akhmetzyanova, C. M. Sawai, D. R. Fooksman, B. Reizis, *Cell Stem Cell* **2020**, *27*, 336.
[86] A. Gomariz, P. M. Helbling, S. Isringhausen, U. Suessbier, A. Becker, A. Boss, T. Nagasawa, G. Paul, O. Goksel, G. Székely, S. Stoma, S. F.

© 2024 The Author(s). Advanced Healthcare Materials published by Wiley-VCH GmbH

21922659, 2024, 22, Downloaded from https://onlinelibrary.wiley.com/doi/10.1002/adhm.202304157 by Karlsruher Institut F., Wiley Online Library on [29/11/2024]. See the Terms and Conditions (https://onlinelibrary.wiley.com/terms-and-conditions) on Wiley Online Library for rules of use; OA articles are governed by the applicable Creative Commons License

Nørrelykke, M. G. Manz, C. Nombela-Arrieta, *Nat. Commun.* **2018**, *9*, 2532.
[87] R. Glass, M. Moller, J. P. Spatz, *Nanotechnology* **2003**, *14*, 1153.
[88] M. V. Tsurkan, K. Chwalek, S. Prokoph, A. Zieris, K. R. Levental, U. Freudenberg, C. Werner, *Adv. Mater.* **2013**, *25*, 2606.
[89] a) K. R. Brown, M. J. Natan, *Langmuir* **1998**, *14*, 726; b) T. Lohmueller, E. Bock, J. P. Spatz, *Adv. Mater.* **2008**, *20*, 2297.
[90] R. Bubeck, C. Bechinger, S. Neser, P. Leiderer, *Phys. Rev. Lett.* **1999**, *82*, 3364.
[91] a) A. Kowalczyk, C. Oelschlaeger, N. Willenbacher, *Meas. Sci. Technol.* **2015**, *26*, 015302; b) J. C. Crocker, D. G. Grier, *J. Colloid Interface Sci.* **1996**, *179*, 298.
[92] D. Wirtz, *Annu. Rev. Biophys.* **2009**, *38*, 301.
[93] I. Petit, M. Szyper-Kravitz, A. Nagler, M. Lahav, A. Peled, L. Habler, T. Ponomaryov, R. S. Taichman, F. Arenzana-Seisdedos, N. Fujii, J. Sandbank, D. Zipori, T. Lapidot, *Nat. Immunol.* **2002**, *3*, 687.
[94] J. D. Brown, H. E. Dillon, D. V. Kaweesa, A. M. Harada, *Biosyst. Eng.* **2017**, *163*, 28.
[95] C. Stringer, T. Wang, M. Michaelos, M. Pachitariu, *Nat. Methods* **2021**, *18*, 100.
[96] A. Waisman, A. M. Norris, M. Elías Costa, D. Kopinke, *Sci. Rep.* **2021**, *11*, 11793.
[97] a) B. Wognum, N. Yuan, B. Lai, C. L. Miller, *Basic Cell Culture Protoc.* **2013**, *946*, 267; b) Culture and Analysis of Hematopoietic Progenitor Cells in CFU Assays | STEMCELL Technologies, https://www.stemcell.com/culture-and-analysis-of-hematopoietic-progenitor-cells-in-cfu-assays.html (accessed: April 2024).

© 2024 The Author(s). Advanced Healthcare Materials published by Wiley-VCH GmbH

21922659, 2024, 22, Downloaded from https://onlinelibrary.wiley.com/doi/10.1002/adhm.202304157 by Karlsruher Institut F., Wiley Online Library on [29/11/2024]. See the Terms and Conditions (https://onlinelibrary.wiley.com/terms-and-conditions) on Wiley Online Library for rules of use; OA articles are governed by the applicable Creative Commons License